Supplementary Information for

Intrinsic metal-support interactions break the activity-stability dilemma in electrocatalysis

Lingxi Zhou[1,5], Menghao Yang[2,5], Yihong Liu[2], Feiyu Kang[3,4], Ruitao Lv[1,4]*

[1]State Key Laboratory of New Ceramics and Fine Processing, School of Materials Science and Engineering, Tsinghua University, Beijing 100084, China.

[2]Shanghai Key Laboratory for R&D and Application of Metallic Functional Materials, School of Materials Science and Engineering, Tongji University, Shanghai 200120, China.

[3]Institute of Materials Research and Shenzhen Geim Graphene Center, Tsinghua Shenzhen International Graduate School, Tsinghua University, Shenzhen 518055, China.

[4]Key Laboratory of Advanced Materials (MOE), School of Materials Science and Engineering, Tsinghua University, Beijing 100084, China.

[5]These authors contributed equally: Lingxi Zhou and Menghao Yang.

*Correspondence to: lvruitao@tsinghua.edu.cn

Table of contents:

Additional Supplementary File:

Supplementary Video 1

Supplementary Code

Supplementary Discussion 1

The concept of the chemical steam deposition (CSD) strategy

The 'bottom-up' approach through assembly at the atomic and molecular scales is an important method for the controllable synthesis of nanomaterial[1,2]. The chemical vapor deposition (CVD) methodology stands out as a preeminent technique for the synthesis of high-purity nanomaterials featuring uniform compositional integrity, achieved through intricate atomic-scale reactions involving gaseous precursors[3,4]. Hydrothermal technology is another 'bottom-up' synthesis approach rooted in solution-phase reactions, utilizing supercritical fluids under high temperature and pressure to synthesize highly dispersed nano-composites[5,6]. We propose a novel hypothesis wherein the integration of hydrothermal reaction conditions with the potential generation of volatile gases could elicit chemical vapor reactions within the gaseous phase. This innovative approach enables direct, in-situ deposition of nanomaterials onto the substrate, effectively bridging the divide between conventional hydrothermal synthesis and the precision of CVD-based techniques. Notably, to our knowledge, this design principle remains unexplored in nanomaterial fabrication. Therefore, the CSD strategy combines the principle of CVD and the conditions of hydrothermal reaction, is proposed and applied in the synthesis of solid solution materials for the first time.

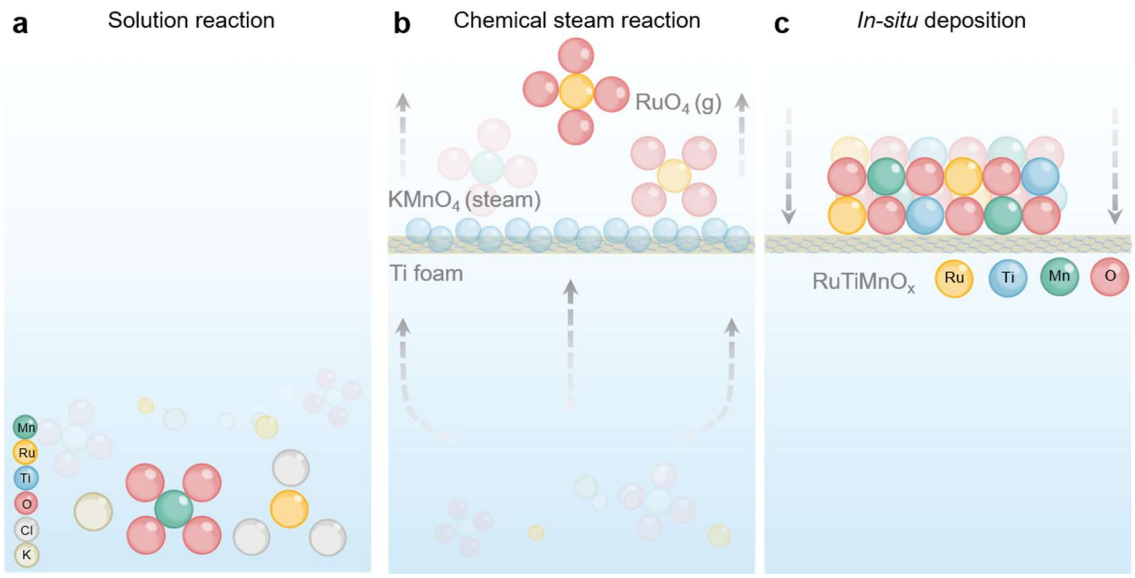

Supplementary Figure 1. Schematic diagram of the mechanism of the chemical steam deposition (CSD) strategy. The one-step method to realize CSD is divided into the following steps: **a**, solution reaction of $KMnO_4$ and $RuCl_3$ to generate RuO_4 gas. **b**, Chemical vapor reaction between the gas-phase $KMnO_4$ and RuO_4 on the Ti foam (TF). **c**, In-situ deposition of $RuTiMnO_x$ solid solution on TF.

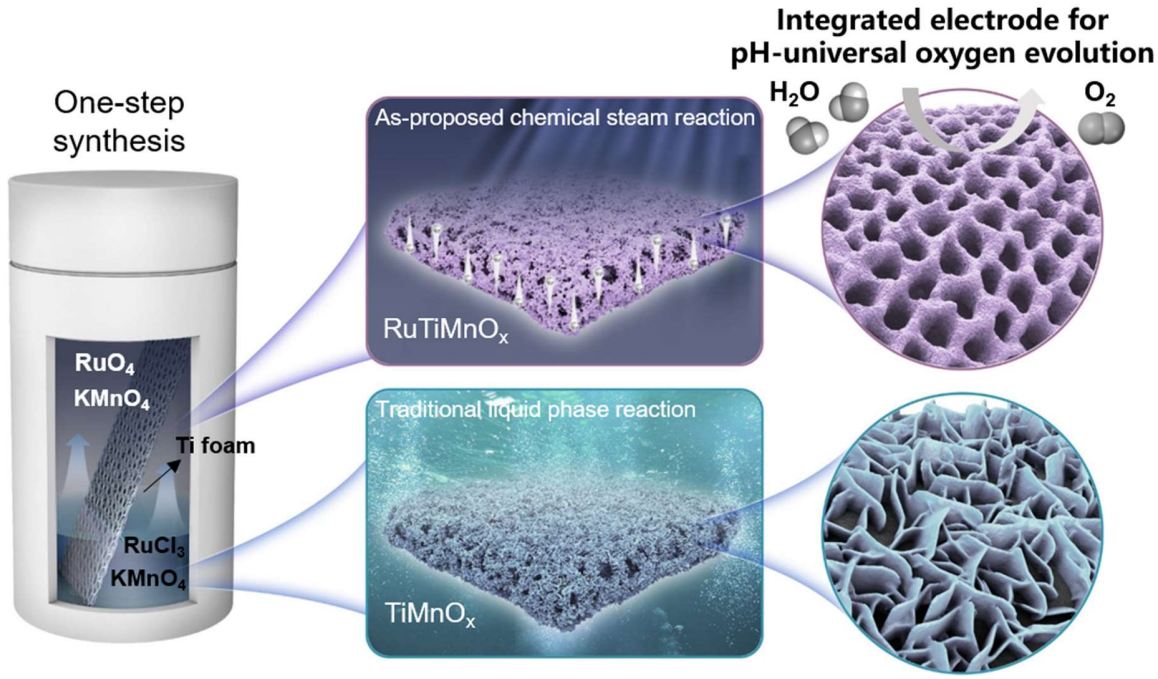

Supplementary Figure 2. Schematic diagram of the one-step synthesis of the integrated $RuTiMnO_x$ electrode through CSD strategy.

*Note: Under hydrothermal conditions, $RuTiMnO_x$ (colored in purple) was obtained via the gas-phase reaction, while $TiMnO_x$ (colored in blue) was obtained in the traditional liquid-phase reaction.

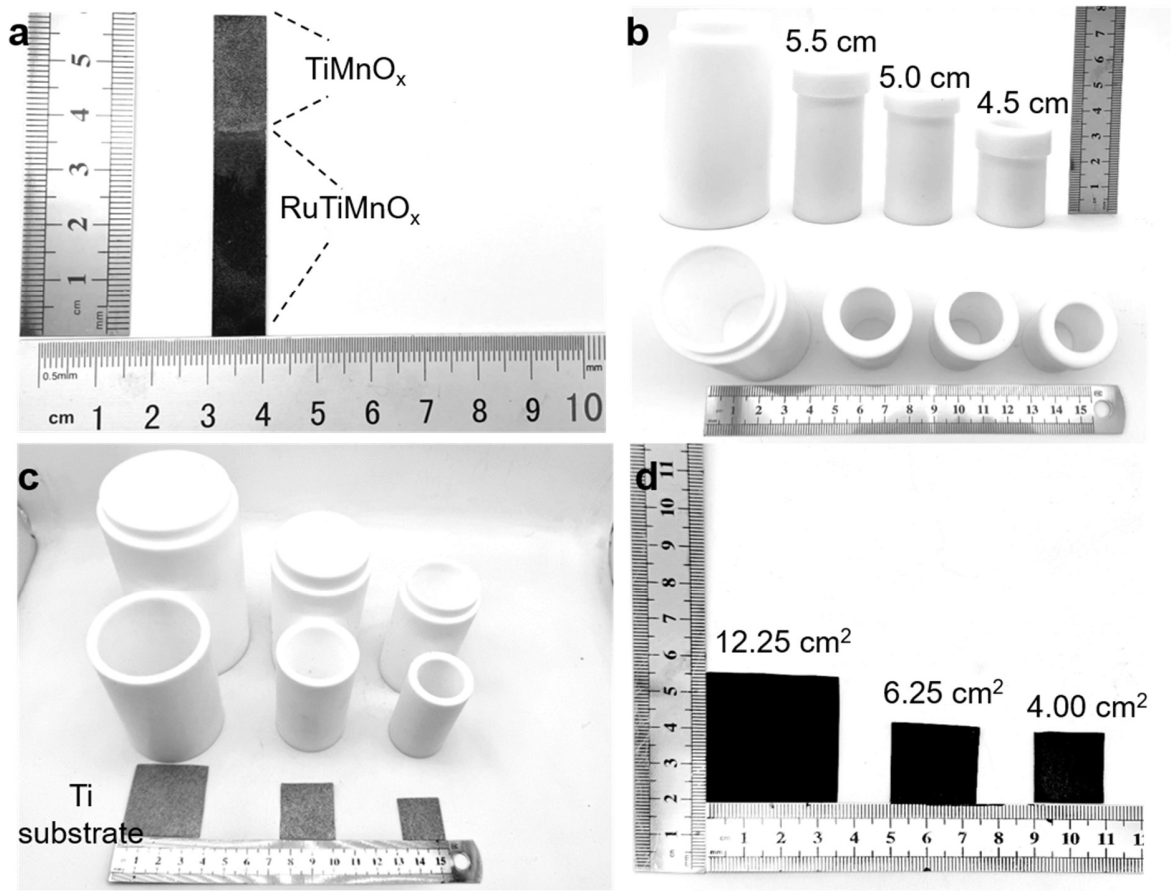

Supplementary Figure 3. Optical photos of the samples and CSD reaction apparatus. a, $TiMnO_x$ and $RuTiMnO_x$ samples. **b**, Hollow supports placed at different heights (4.5, 5.0 and 5.5 cm) within the polytetrafluoroethylene (PTFE) lining of the reaction kettle. **c**, Reaction kettle linings with different volumes (50, 100 and 200 mL) and corresponding hollow supports. **d**, $RuTiMnO_x$ electrodes of different sizes (4.00, 6.25 and 12.25 cm^2) obtained from the reactors in (**c**).

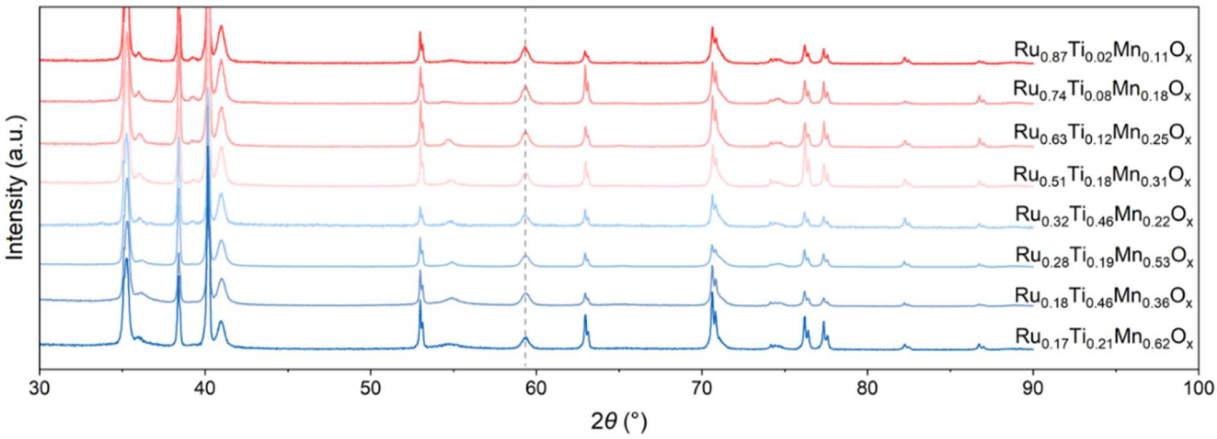

Supplementary Figure 4. Phase characterization of as-prepared $RuTiMnO_x$ electrode. X-Ray diffraction (XRD) patterns of $RuTiMnO_x$ with different Ru, Ti, and Mn ratios. As the Ru ratio increases (from bottom to top), the peak of $RuTiMnO_x$ located at 59.3° shifts to a lower angle, indicating the successful incorporation of Ru into the lattice.

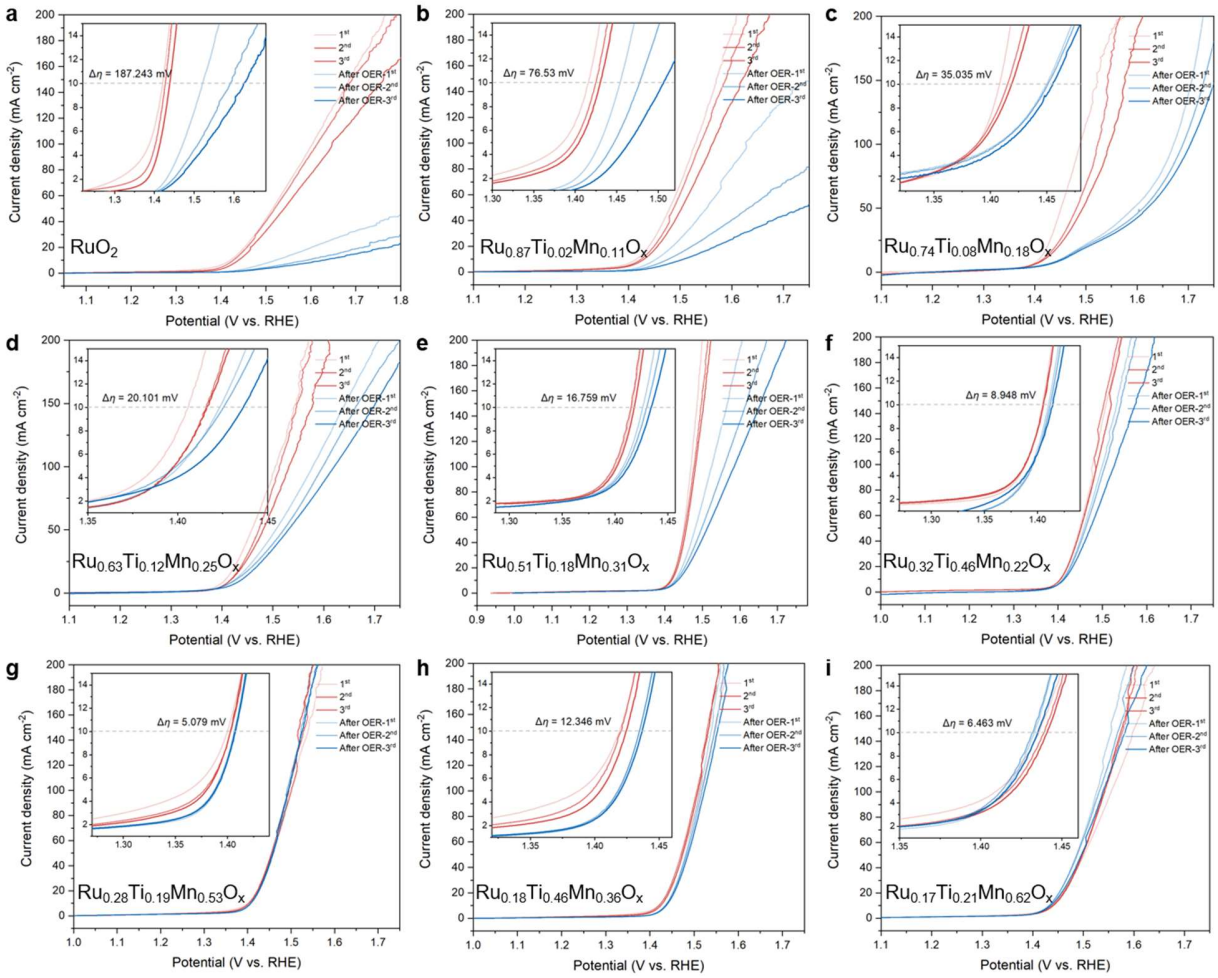

Supplementary Figure 5. OER activity of as-prepared $RuTiMnO_x$ electrode. a–i, Linear sweep voltammetry (LSV) curves of RuO_2 and $RuTiMnO_x$ with different ratios in 0.5 M H_2SO_4.

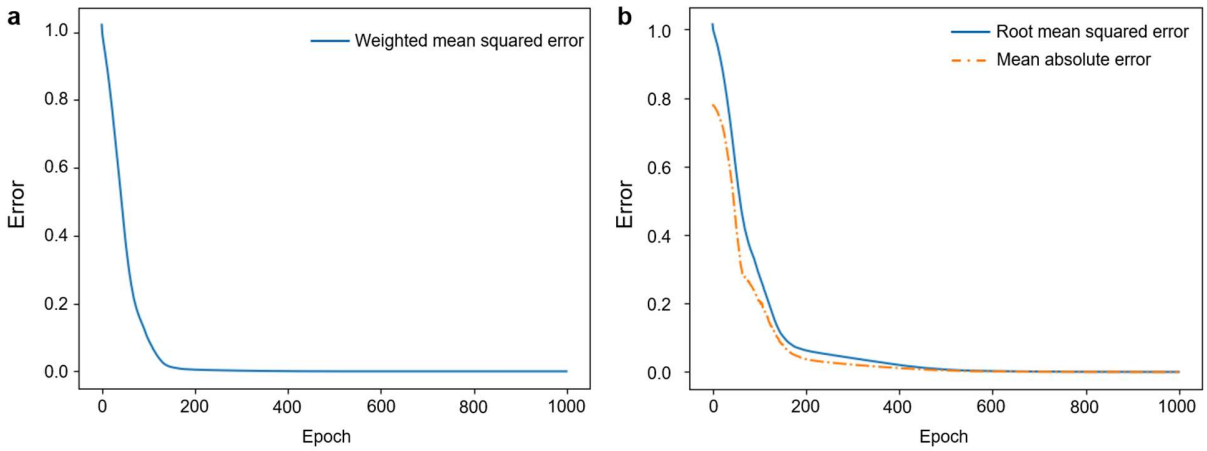

Supplementary Figure 6. The machine learning process. a,**b**, The loss function, namely the weighted mean squared error, of overpotential (η) and the degradation rate (ΔE) (**a**) and the root mean squared error along with mean absolute error (**b**).

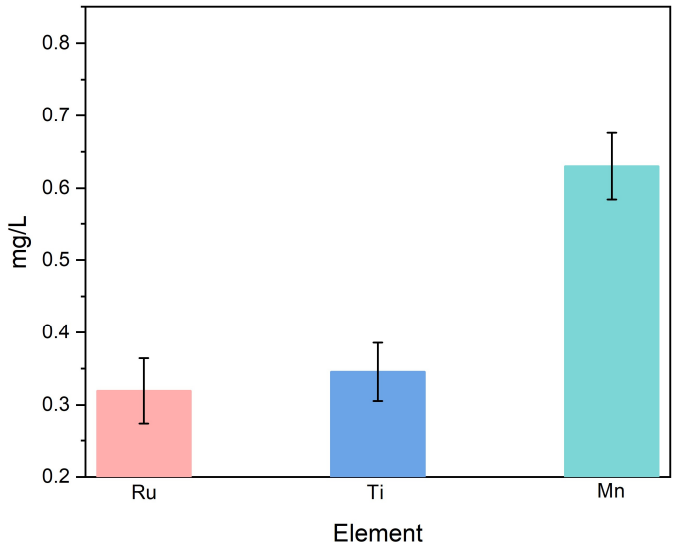

Supplementary Figure 7. Element ratio analysis of the as-prepared $RuTiMnO_x$ electrode.

Note: Inductively coupled plasma optical emission spectrometry (ICP-OES) analysis data of the elemental concentration in $Ru_{0.24}Ti_{0.28}Mn_{0.48}O$. Since $RuTiMnO_x$ was grown in situ on a Ti substrate, the dissolution of the solid did not allow for the measurement of the Ti content in the $RuTiMnO_x$. To ascertain the relative elemental proportions within the $RuTiMnO_x$ material, we implemented an ultrasonic dispersion technique to disperse the $RuTiMnO_x$ in an aqueous medium, subsequently quantifying the elemental composition of the resultant solution through ICP-OES.

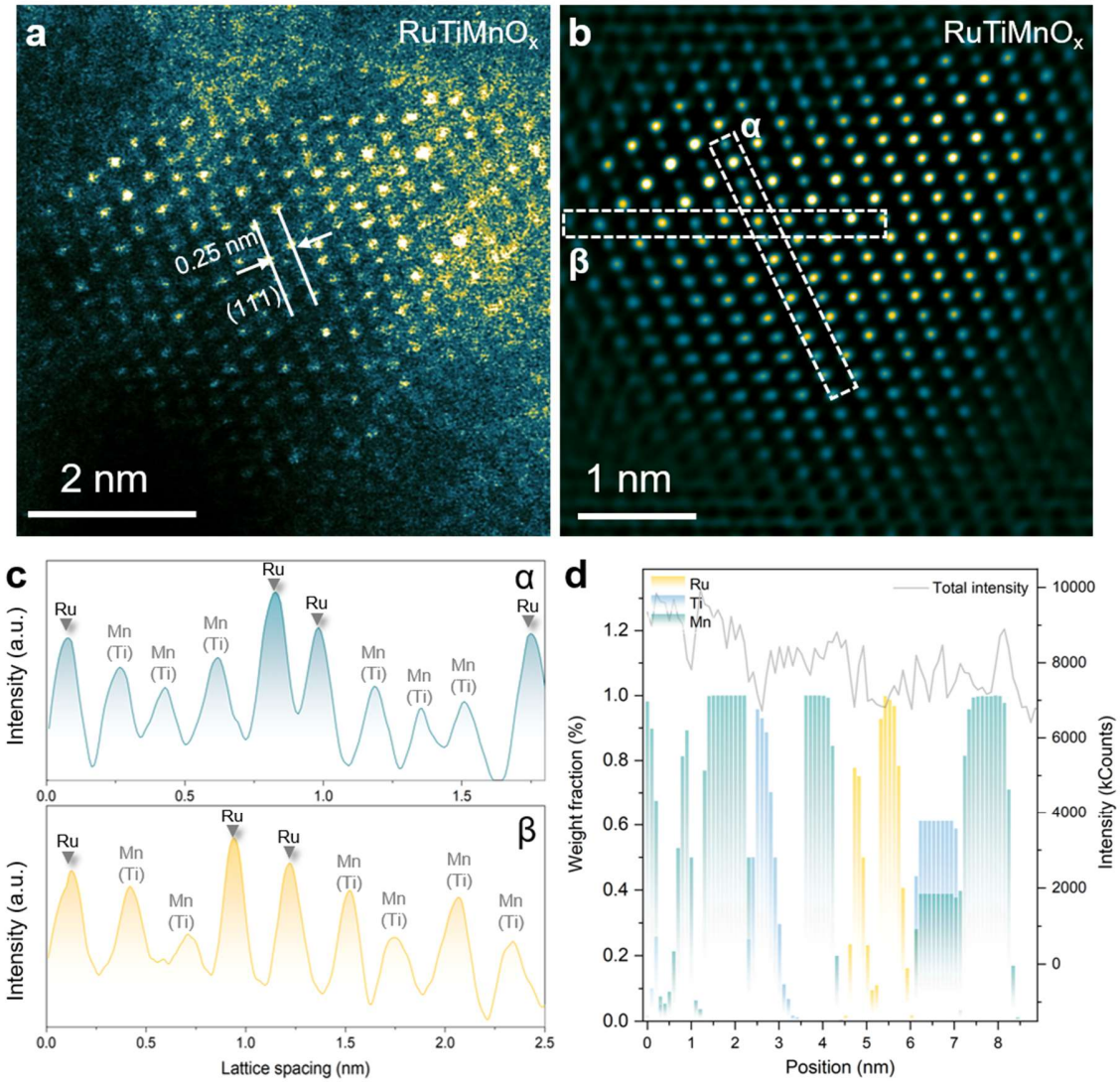

Supplementary Figure 8. Structure characterizations of as-synthesized $RuTiMnO_x$. a, Aberration-corrected high-angle annular dark field scanning transmission electron microscopy (HAADF-STEM) image of $Ru_{0.24}Ti_{0.28}Mn_{0.48}O$. **b**, Inverse-fast Fourier-transform (IFFT) image for (**a**). **c**, STEM intensity profiles presented to directions labelled with blue (α) and red (β) boxs. **d**, Weight fraction and total intensity profiles presented to direction labelled with α box.

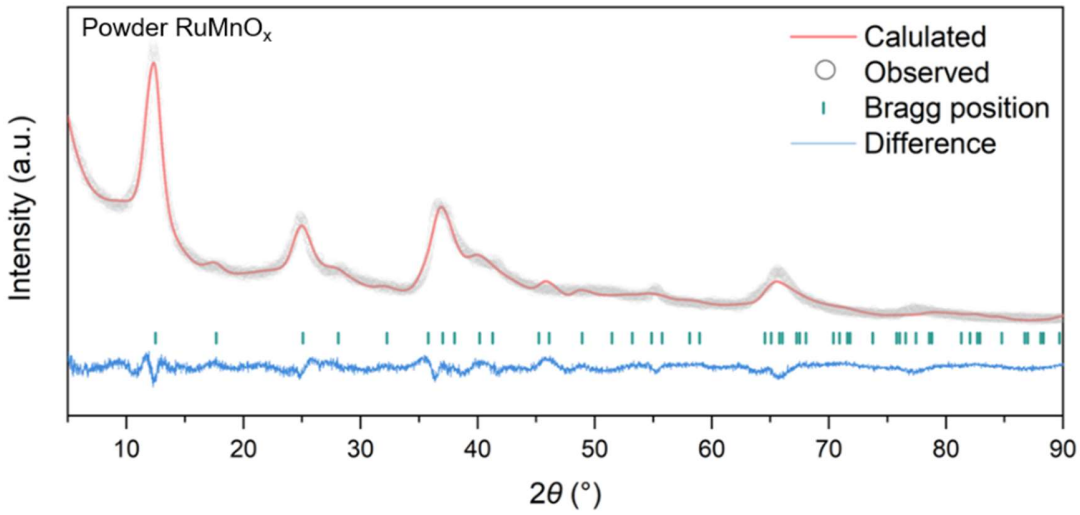

Supplementary Figure 9. Rietveld refinement analysis of XRD patterns of $Ru_{0.56}Mn_{0.44}O_2$.

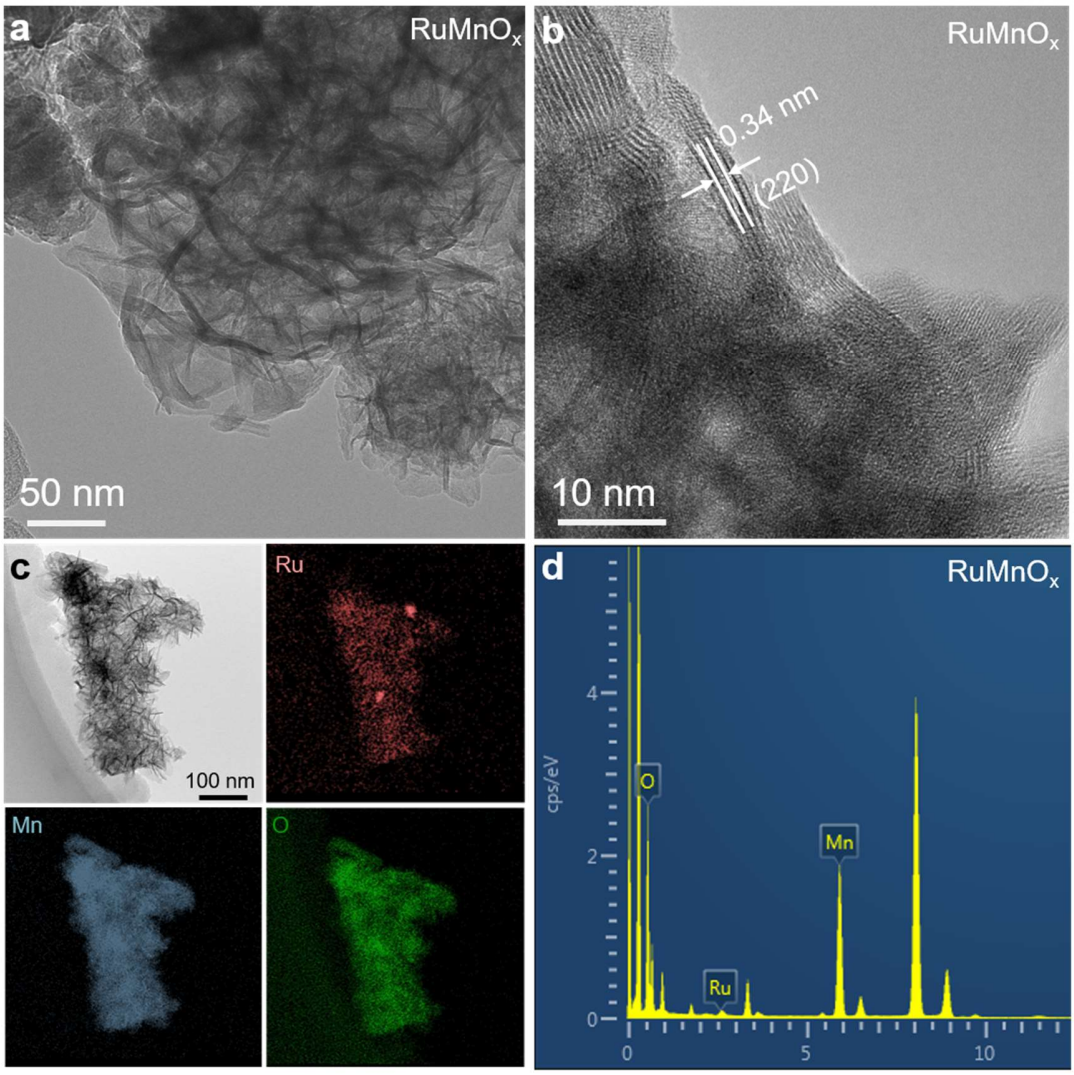

Supplementary Figure 10. Structure characterizations of as-synthesized $RuMnO_x$. a,**b**, transmission electron microscopy (TEM) images at different magnifications. **c**, TEM image and the corresponding elemental mapping profile of Ru (red), Mn (blue) and O (green). **d**, Energy dispersive X-ray spectroscopy (EDX) spectra.

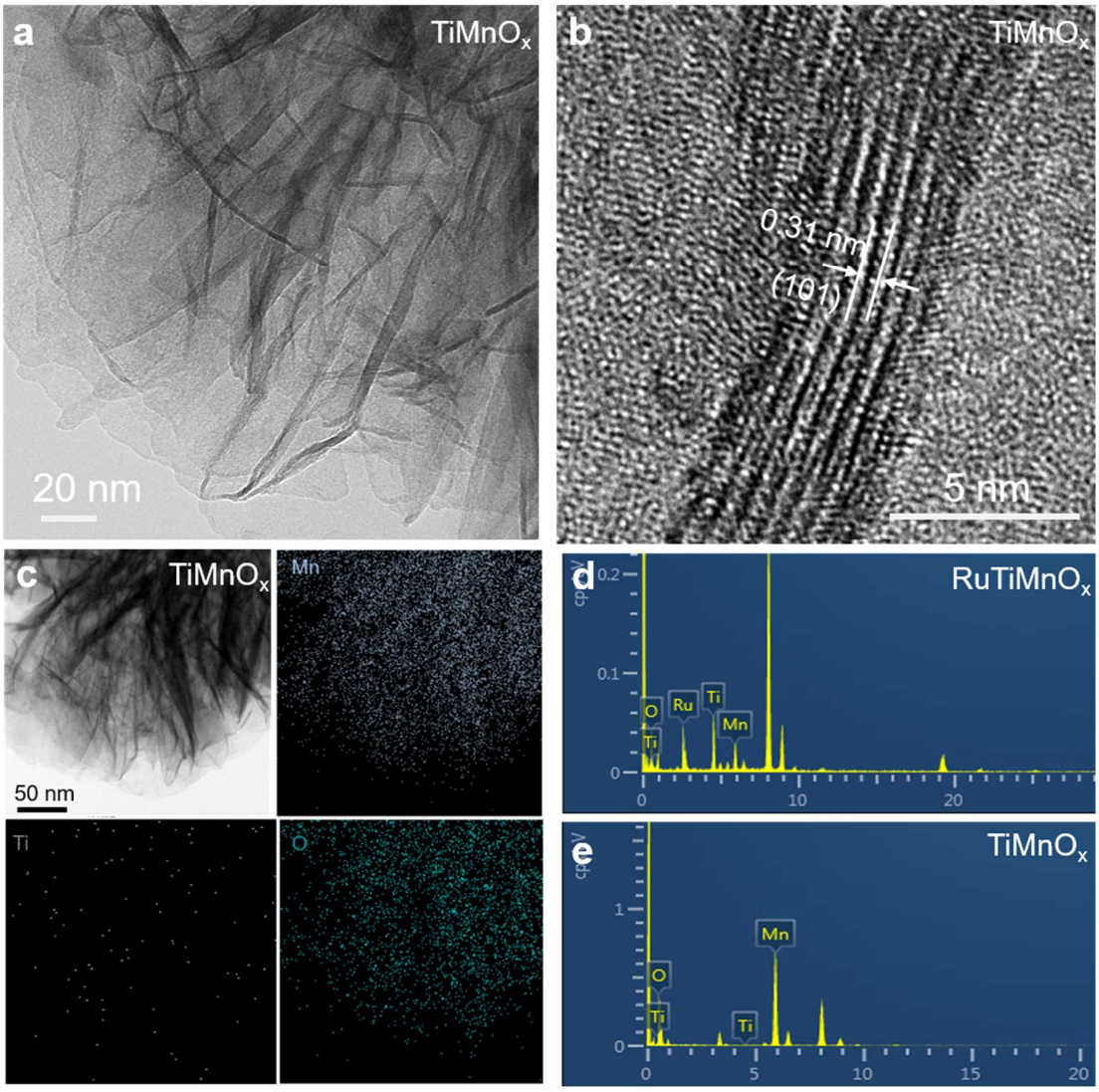

Supplementary Figure 11. Structure characterizations of as-synthesized $TiMnO_x$. a,**b**, TEM images at different magnifications. **c**, TEM image and the corresponding elemental mapping profile of Mn (blue), Ti (gray) and O (green). **d**,**e**, EDX spectra of $RuTiMnO_x$ (**d**) and $TiMnO_x$ (**e**).

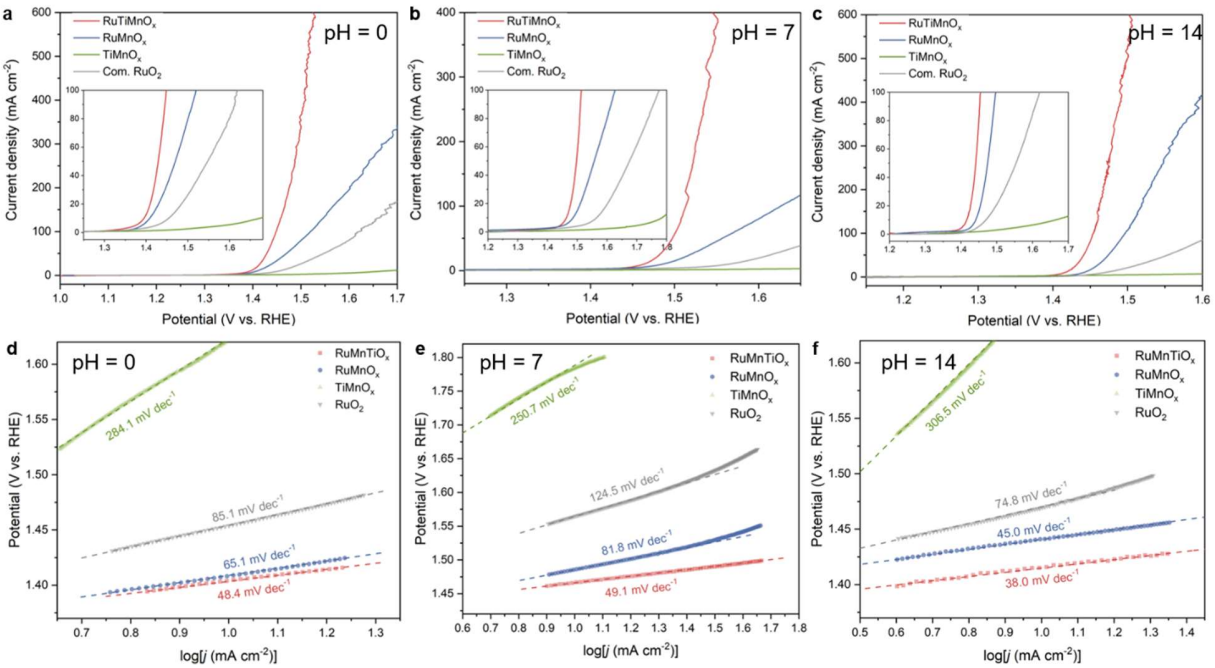

Supplementary Figure 12. OER activity evaluation. a–c, LSV curves of $RuTiMnO_x$, $RuMnO_x$, MnO_x, and commercial RuO_2 (Com. RuO_2) in 0.5 M H_2SO_4 (pH=0) (**a**), 0.5 M PBS (pH=7) (**b**), and 1.0 M KOH (pH=14) (**c**). **d–f**, Tafel plots derived from the LSV curves in pH=0 (**d**), pH=7 (**e**) and pH=14 (**f**).

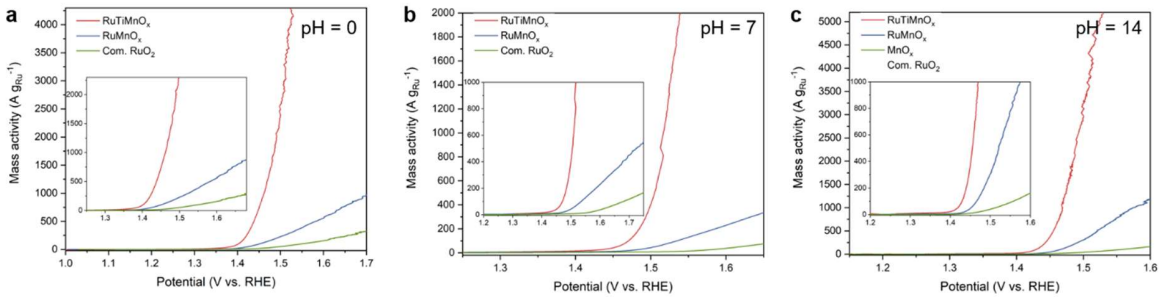

Supplementary Figure 13. OER intrinsic activity evaluation. a–**c**, Mass activity curves of $RuTiMnO_x$, $RuMnO_x$, and Com. RuO_2 in 0.5 M H_2SO_4 (pH=0) (**a**), 0.5 M PBS (pH=7) (**b**), and 1.0 M KOH (pH=14) (**c**).

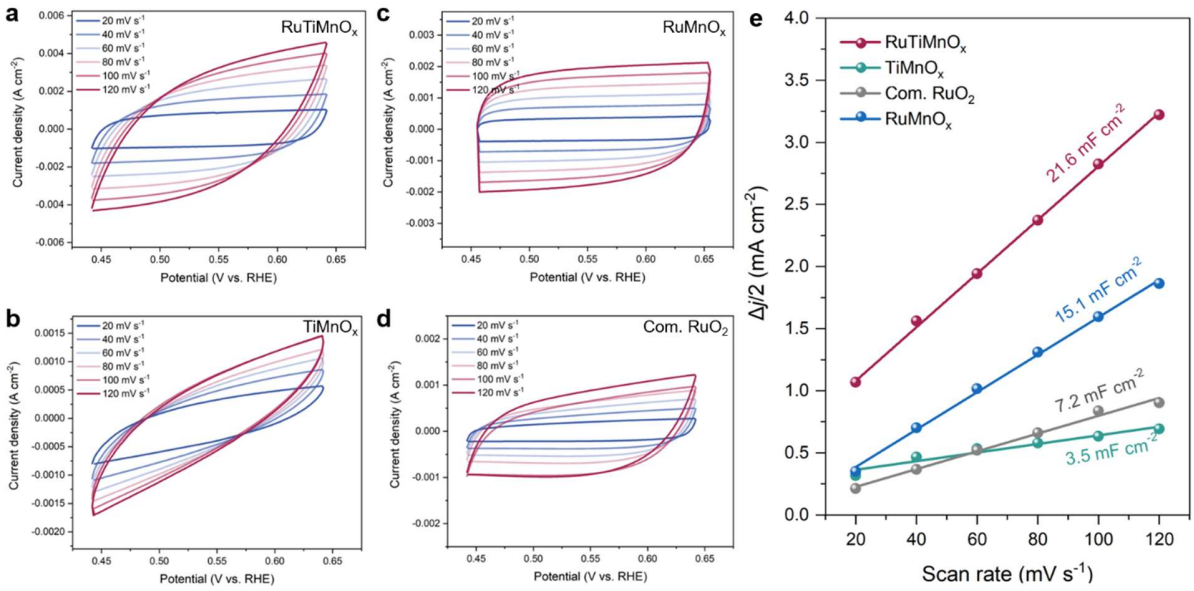

Supplementary Figure 14. Electrochemically active surface area (ECSA) measurement. a–d, Cyclic voltammetry (CV) curves of $RuTiMnO_x$ (**a**), $TiMnO_x$ (**b**), $RuMnO_x$ (**c**), and Com. RuO_2 (**d**) in the potential range of 0.45~0.65 V vs. RHE with the scanning rates of 20~120 mV s^{-1}. **e**, Linear relationships between current density (*j*) and scan rate, the C_{dl} are absolute value of the slope of the liner fits to the data.

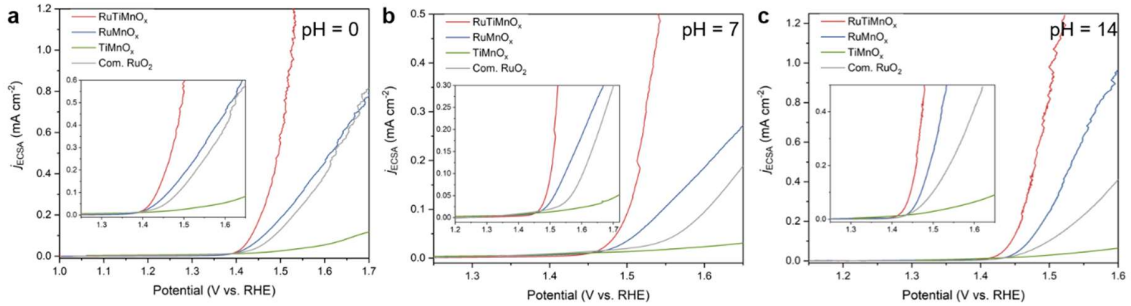

Supplementary Figure 15. OER specific activity evaluation. a–**c**, ECSA-normalized LSV curves of $RuTiMnO_x$, $TiMnO_x$, $RuMnO_x$, and Com. RuO_2 in 0.5 M H_2SO_4 (pH=0) (**a**), 0.5 M PBS (pH=7) (**b**), and 1.0 M KOH (pH=14) (**c**).

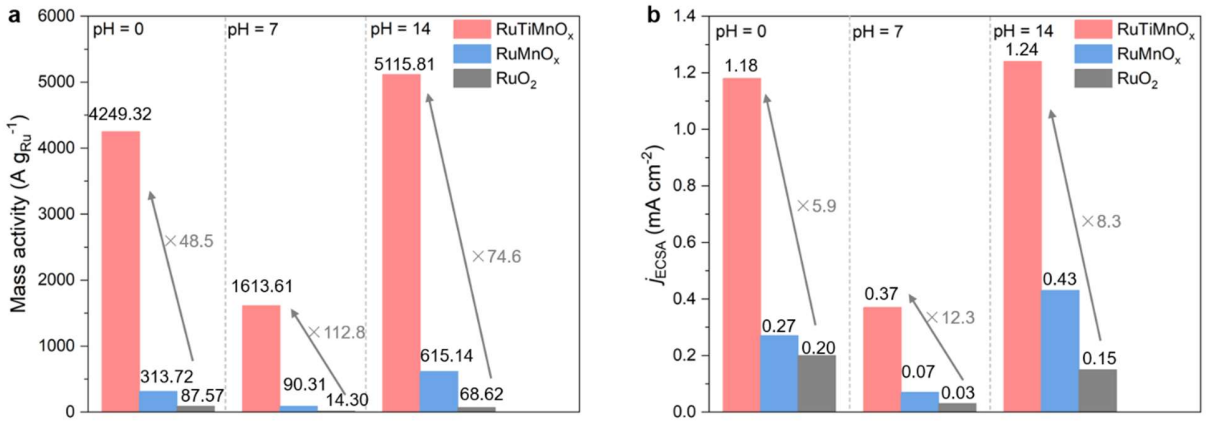

Supplementary Figure 16. OER intrinsic activity comparison. a,**b**, OER intrinsic activity comparison of $RuTiMnO_x$, $RuMnO_x$, and Com. RuO_2 in 0.5 M H_2SO_4 (pH=0), 0.5 M PBS (pH=7), and 1.0 M KOH (pH=14), respectively. **a**, Mass activity comparison at 1.53 V vs. RHE. **b**, ECSA-normalized current densities (j_{ECSA}) at 1.53 V vs. RHE.

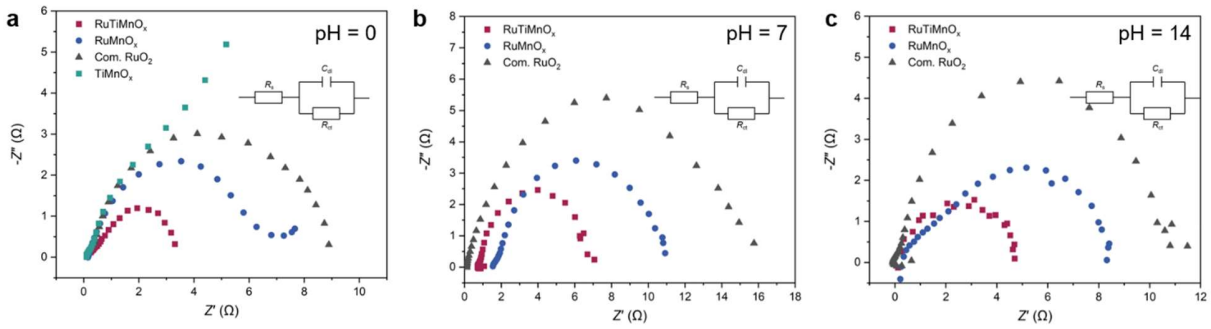

Supplementary Figure 17. Electrochemical impedance analysis. a–c, Electrochemical impedance spectroscopy (EIS) of $RuTiMnO_x$, $RuMnO_x$, and Com. RuO_2 in 0.5 M H_2SO_4 (pH=0) (**a**), 0.5 M PBS (pH=7) (**b**), and 1.0 M KOH (pH=14) (**c**), respectively.

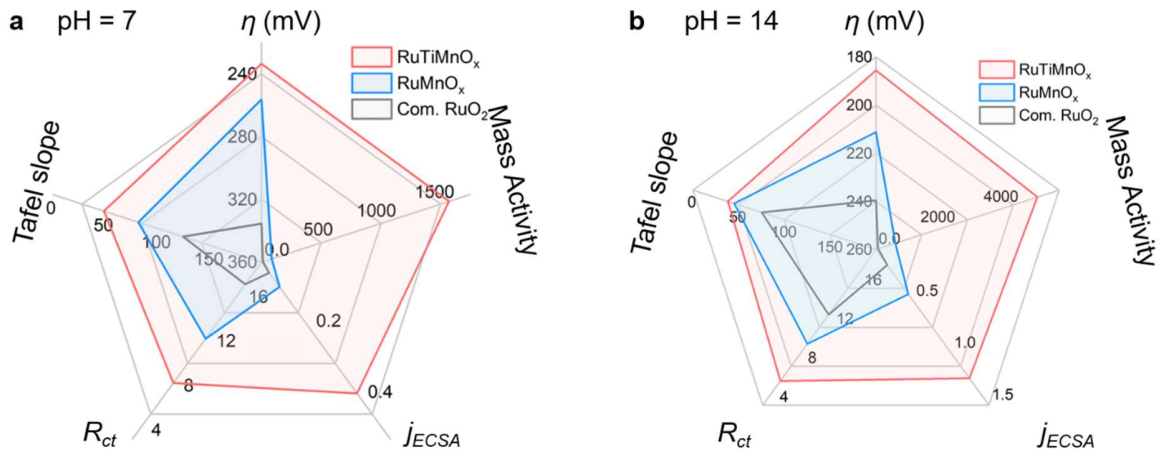

Supplementary Figure 18. Radar plot summarizing different electrochemical activity indicators. a,**b**, Radar plot comparing the OER performance of $RuTiMnO_x$ and the reference samples in 0.5 M PBS (pH=7) (**A**), and 1.0 M KOH (pH=14) (**B**).

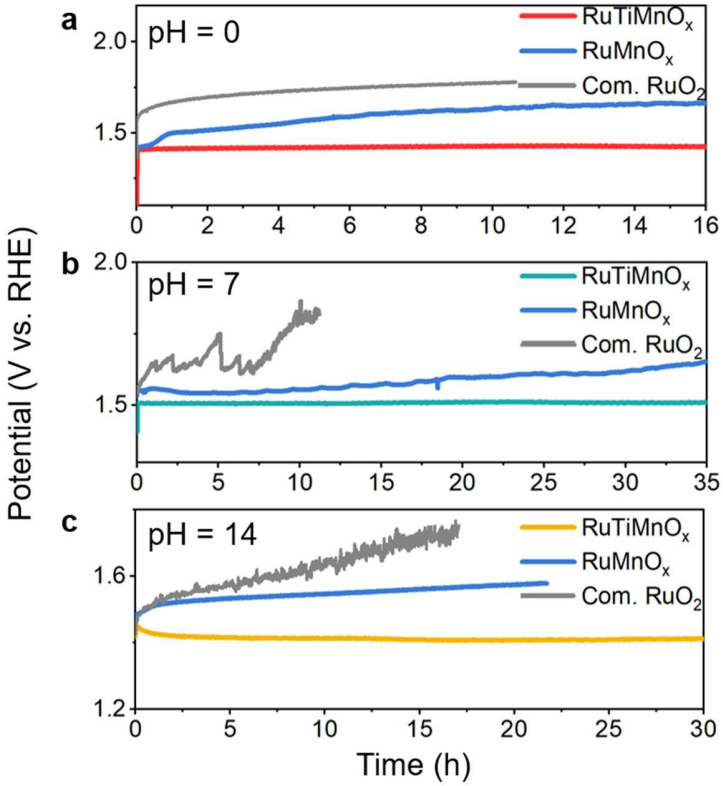

Supplementary Figure 19. OER stability evaluation. a–**c**, Chronoamperometric curves obtained at a current density of 10 mA cm^{-2} for the $RuTiMnO_x$, $RuMnO_x$, and Com. RuO_2 in 0.5 M H_2SO_4 (pH=0) (**a**), 0.5 M PBS (pH=7) (**b**), and 1.0 M KOH (pH=14) (**c**), respectively.

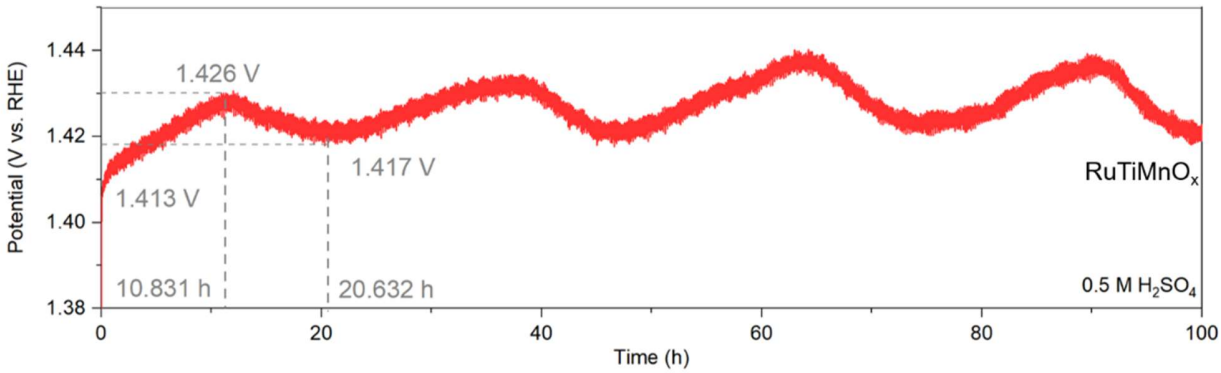

Supplementary Figure 20. OER stability of $RuTiMnO_x$ in the first 100 hours. a–c, Chronoamperometric curve obtained at a current density of 10 mA cm^{-2} for the $RuTiMnO_x$ in the first 100 h in 0.5 M H_2SO_4. Related to Fig. 3C. The voltage exhibited periodic fluctuations. In the first period, the potential increased from 1.413 V to 1.426 V by 0.019 V vs. RHE over ~10.831 hours and then decreased back to 1.417 V vs. RHE over the next ~9.801 hours.

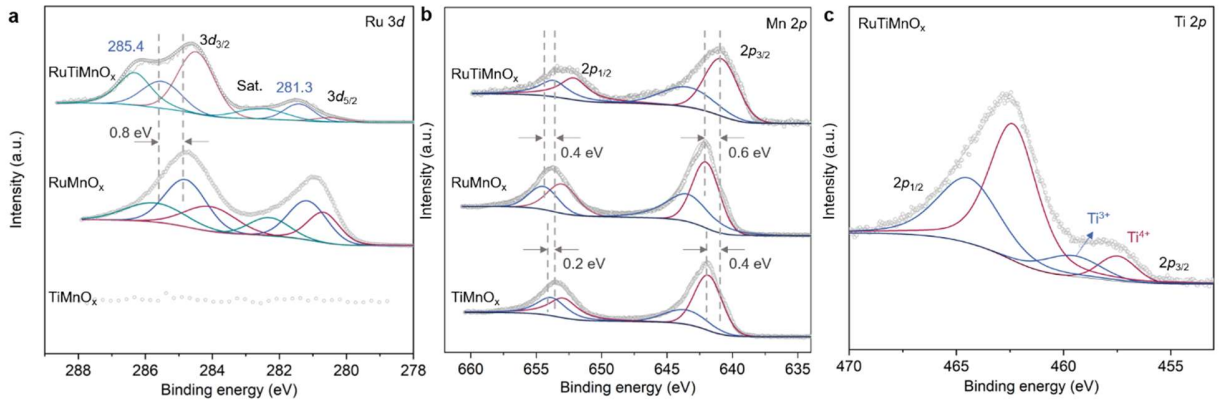

Supplementary Figure 21. X-ray photoelectron spectroscopy (XPS) analysis. a–**c**, XPS spectra of Ru 3*d* (**a**), Mn 2*p* (**b**) and Ti 2*p* (**c**).

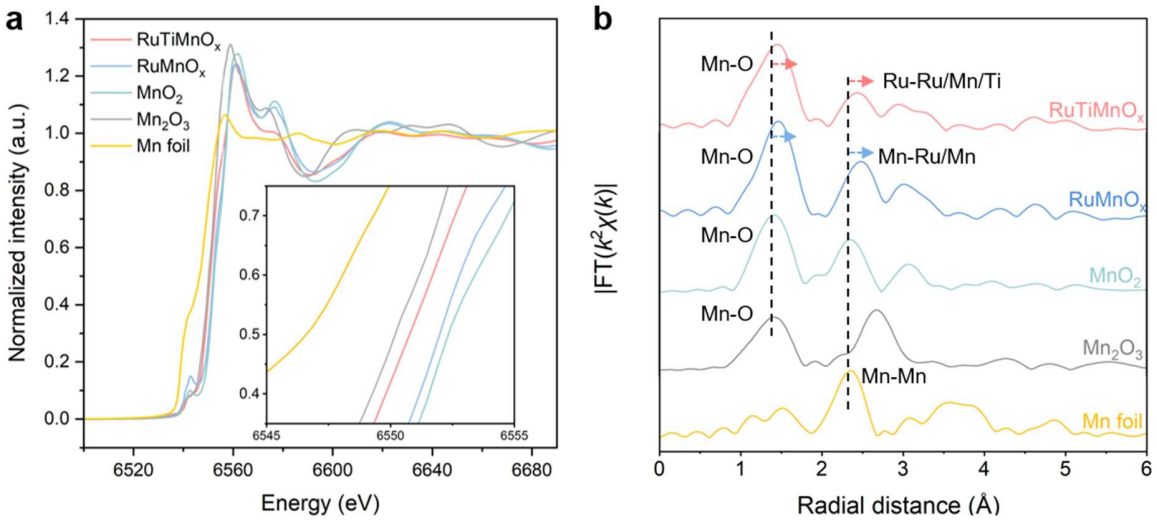

Supplementary Figure 22. X-ray absorption spectroscopy (XAS) study of RuTiMnO$_x$ at Mn K-edge. a, Mn K-edge synchrotron-based X-ray absorption near-edge structure (XANES) spectra of RuTiMnOx. **b**, Fourier-transformed (FT) k^3-weighted $\chi(k)$-function of the extended X-ray absorption fine-structure (EXAFS) spectra for the Mn K-edge. Mn foil, Mn_2O_3 and MnO_2 are used as the references.

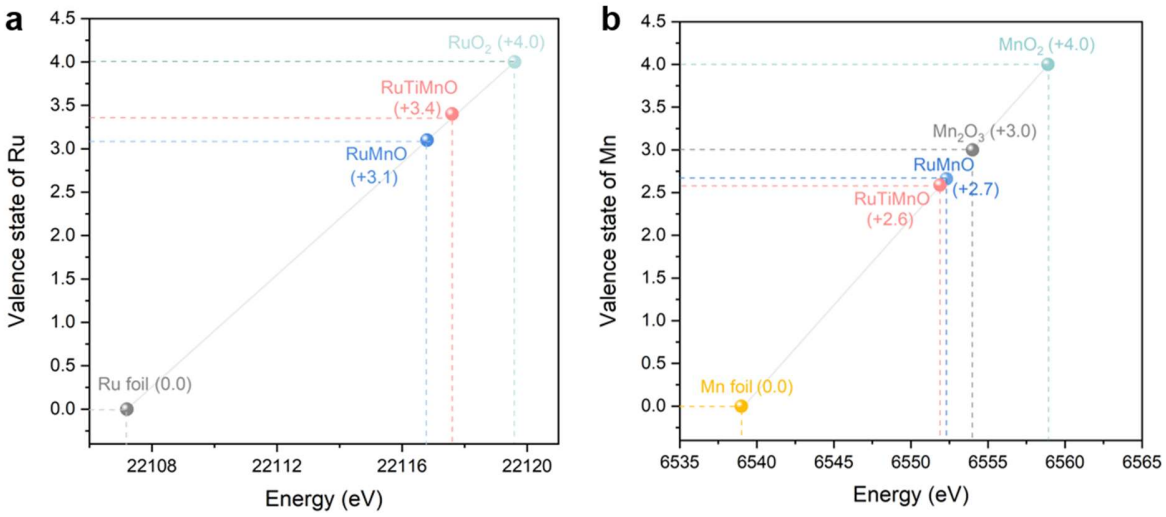

Supplementary Figure 23. Valence state analysis based on XANES results. Relation between the Ru K-edge (**a**) and Mn K-edge (**b**) absorption energy (E_0) and valence states for the $RuTiMnO_x$, $RuMnO_x$ and references. See Supplementary Tables 9 and 10 for details.

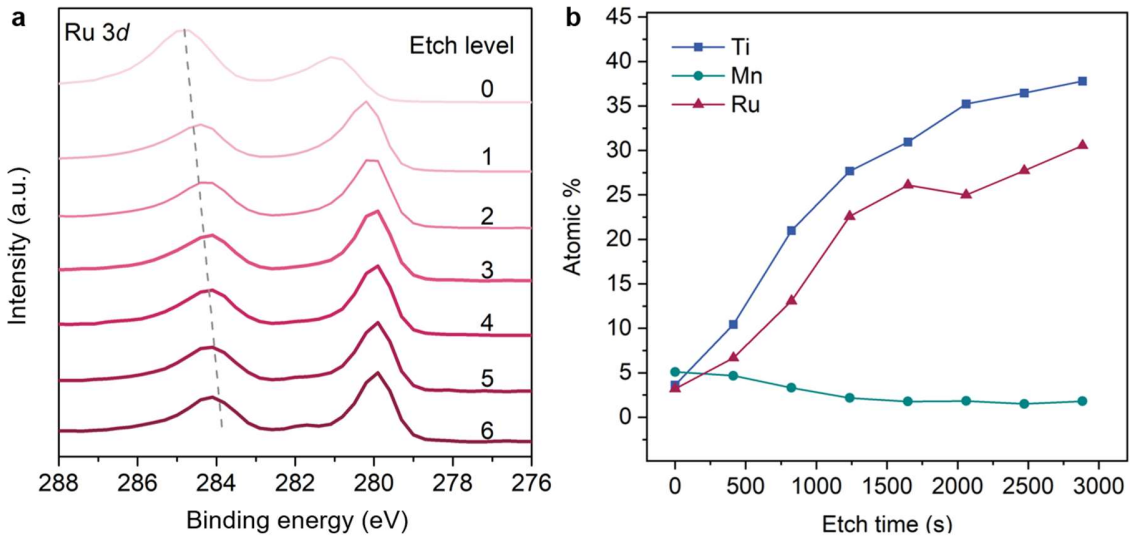

Supplementary Figure 24. In-depth XPS analysis of the RuTiMnO$_x$. a, Depth profile of Ru 3*d* spectra. **b**, The variation of atomic ratio of elements (Ru, Ti and Mn) with etching time.

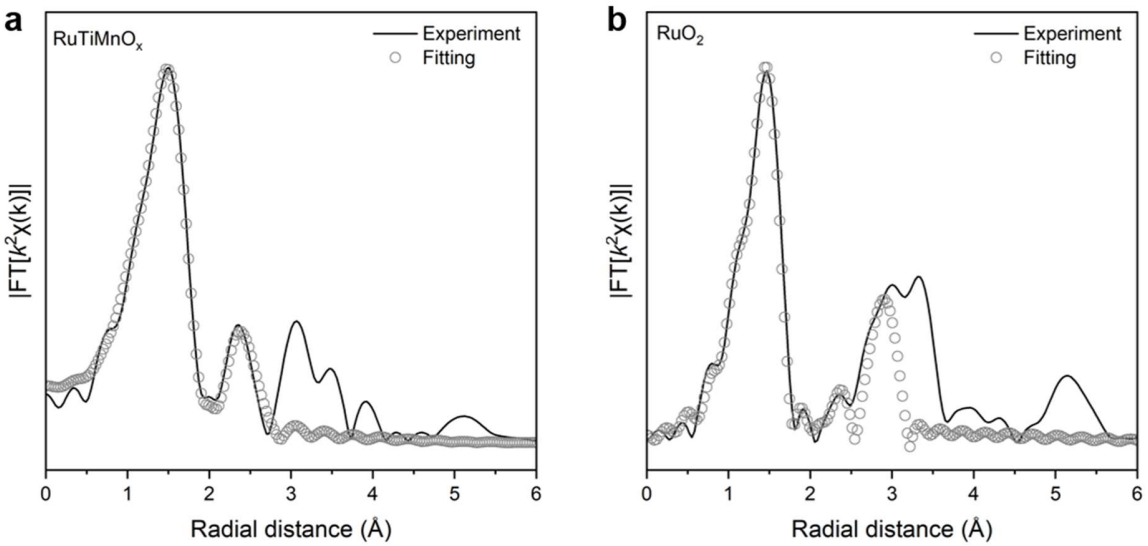

Supplementary Figure 25. The EXAFS curve analysis. a, The EXAFS curve of the Ru K-edge experimental data (solid line) and fitting result (circle) for the $RuTiMnO_x$. **b**, FT-EXAFS curve (solid line) with fitting result (circle). See Supplementary Table 11 for details.

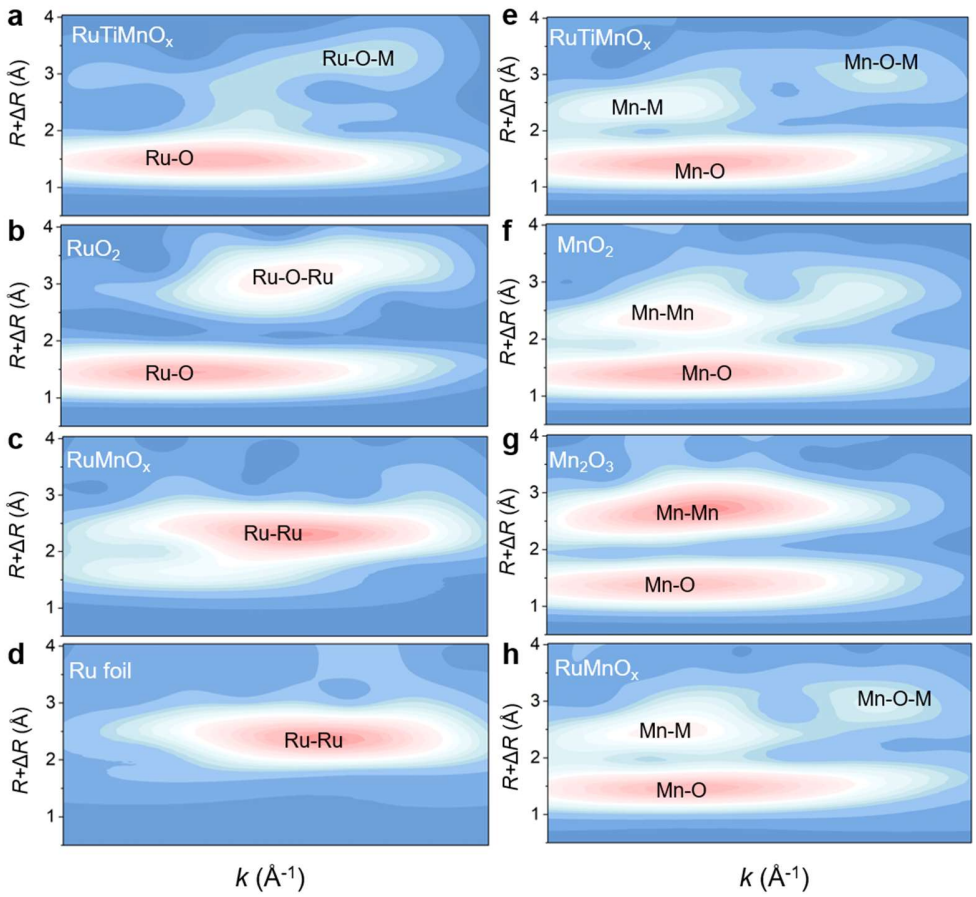

Supplementary Figure 26. Wavelet transforms (WT) for the k^3-weighted EXAFS analysis. a–d, Ru K-edge WT-EXAFS spectra of $RuTiMnO_x$ (**a**), RuO_2 (**b**), $RuMnO_x$ (**c**), and Ru foil (**d**). **e–h**, Mn K-edge WT-EXAFS spectra of $RuTiMnO_x$ (**e**), MnO_2 (**f**), Mn_2O_3 (**g**), and $RuMnO_x$ (**h**).

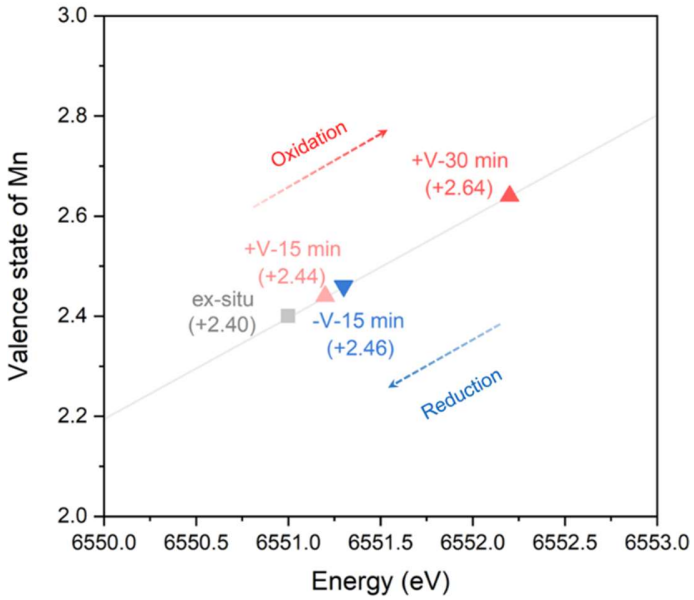

Supplementary Figure 27. Valence state analysis based on in-situ XAS results.

Relation between the Mn K-edge E_0 and valence states for the $RuTiMnO_x$ at different operation conditions. See Supplementary Table 12 for details. During electrolysis under positive voltage, the valence state of Mn gradually increased from +2.40 to +2.64. When a negative voltage was applied, the valence state of Mn reverted to +2.46, close to its initial value, indicating the reversibility of Mn's valence state.

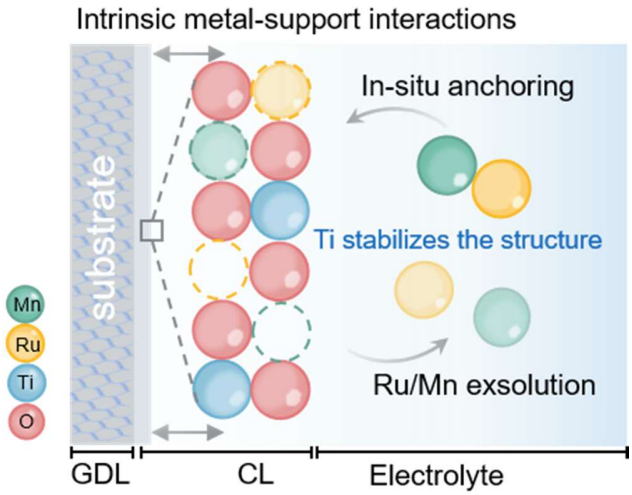

Supplementary Figure 28. Schematic illustration for the stability mechanism of integrated $RuTiMnO_x$ electrode.

We postulate that the stability of $RuTiMnO_x$ originates from both structural stability and compositional stability, where Ti stabilizes the crystal structure and Ru/Mn is anchored in situ after dissolution. GDL denotes gas diffusion layer, CL denotes catalyst layer.

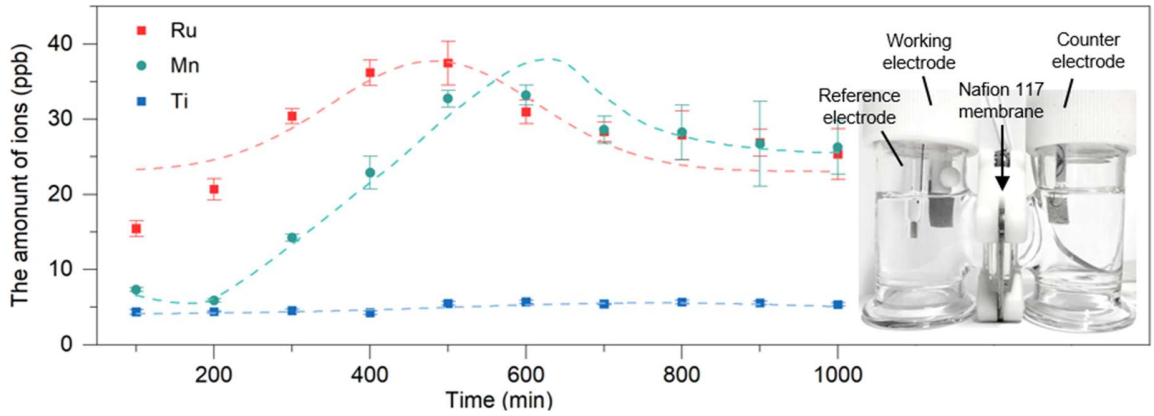

Supplementary Figure 29. Dependence of the Ru, Mn and Ti concentration in the electrolyte at the working electrode side (anode) on the OER reaction time.

OER was conducted under constant current density of 10 mA cm^{-2} in 0.5 M H_2SO_4 electrolyte. A photograph of a homemade H-type cell is shown in the inset.

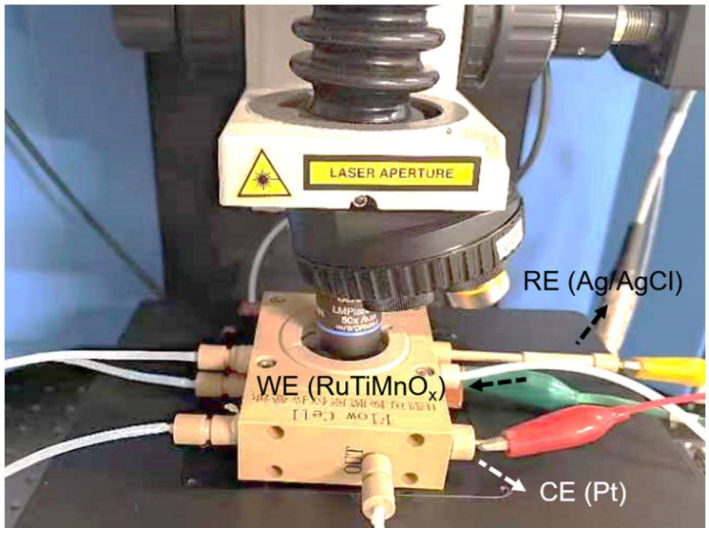

Supplementary Figure 30. Photograph of the in-situ Raman testing apparatus.

RE, WE and CE denote reference electrode, working electrode, and counter electrode, respectively. See Methods for details.

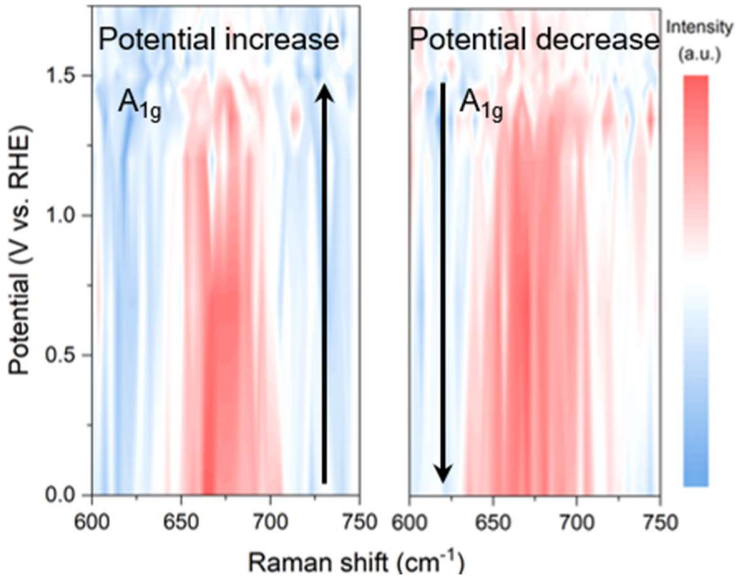

Supplementary Figure 31. 2D in-situ Raman contour image.

The image is enlarged from Fig. 4a.

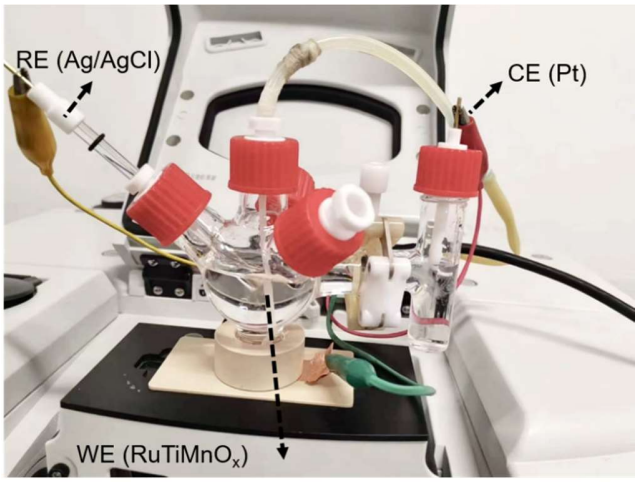

Supplementary Figure 32. Photograph of the in-situ attenuated total reflectance Fourier transform infrared (ATR-FTIR) testing apparatus.

RE, WE and CE denote reference electrode, working electrode, and counter electrode, respectively. See Methods for details.

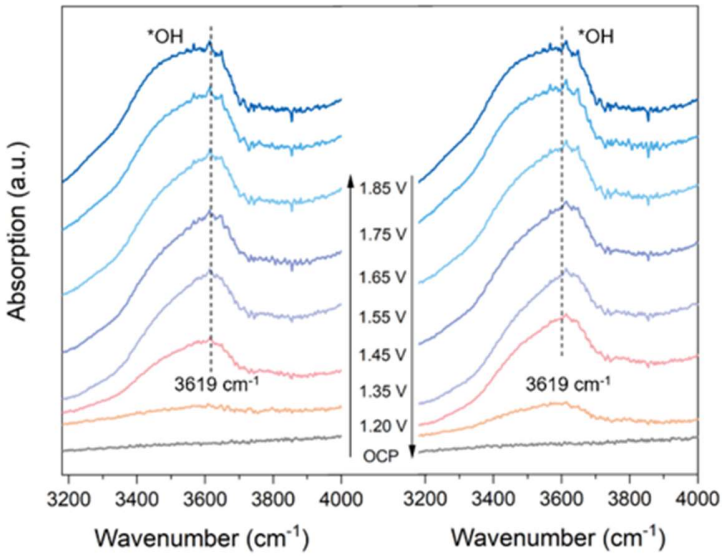

Supplementary Figure 33. In-situ ATR-FTIR spectra.

In-situ ATR-FTIR spectra recorded in the potential range of OCP-1.85 V vs. RHE for $RuTiMnO_x$ in 0.5 M H_2SO_4 electrolyte, with a wavenumber range of 3200-4000 cm^{-1}.

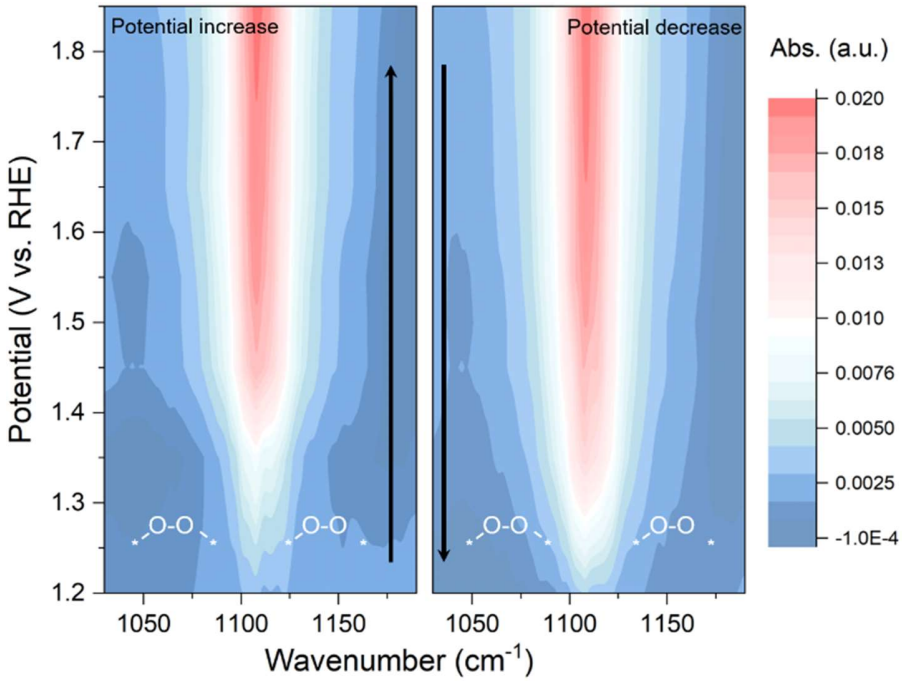

Supplementary Figure 34. 2D In-situ ATR-FTIR spectra contour image.

2D In-situ ATR-FTIR spectra contour image (enlarged from Fig. 4b) recorded in the potential range of OCP-1.85 V vs. RHE for $RuTiMnO_x$ in 0.5 M H_2SO_4 electrolyte.

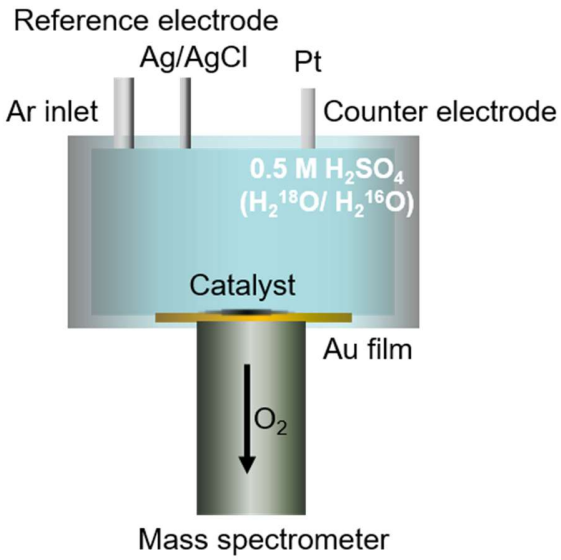

Supplementary Figure 35. Schematic illustration of the in-situ differential electrochemical mass spectrometry (DEMS).

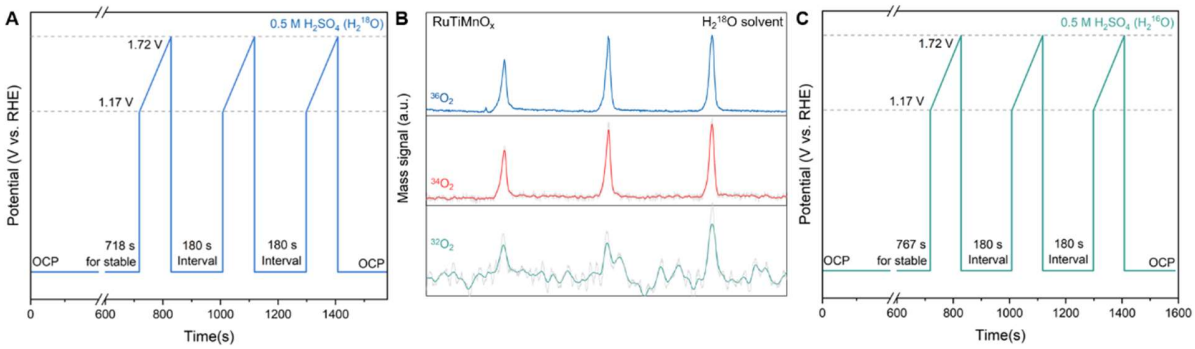

Supplementary Figure 36. The in-situ DEMS analysis. a,**c**, The applied potential as a function of time during in-situ DEMS measurement in 0.5 M H_2SO_4 ($H_2{}^{18}O$) (**a**) and 0.5 M H_2SO_4 ($H_2{}^{16}O$) (**c**). **b**, In-situ DEMS signals of O_2 products for $RuTiMnO_x$ in 0.5 M H_2SO_4 ($H_2{}^{18}O$). See Methods for details.

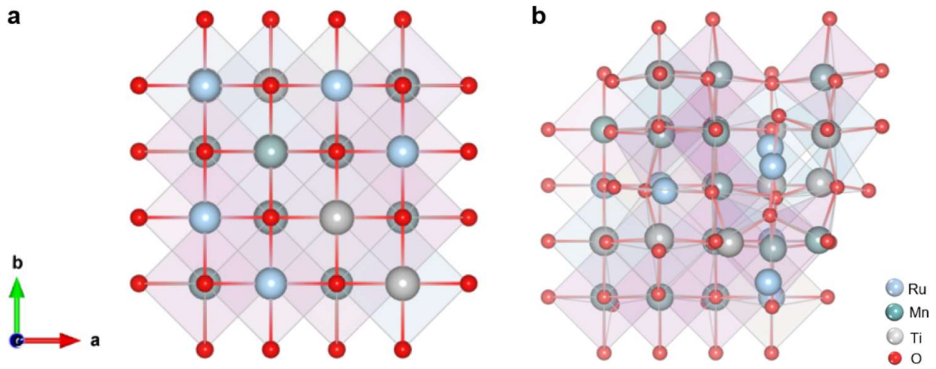

Supplementary Figure 37. $RuTiMnO_x$ catalyst model for first principles calculations. a,**b**, Atomic structure of as-constructed (**a**) and optimized (**b**) $Ru_{0.24}Ti_{0.28}Mn_{0.48}O$.

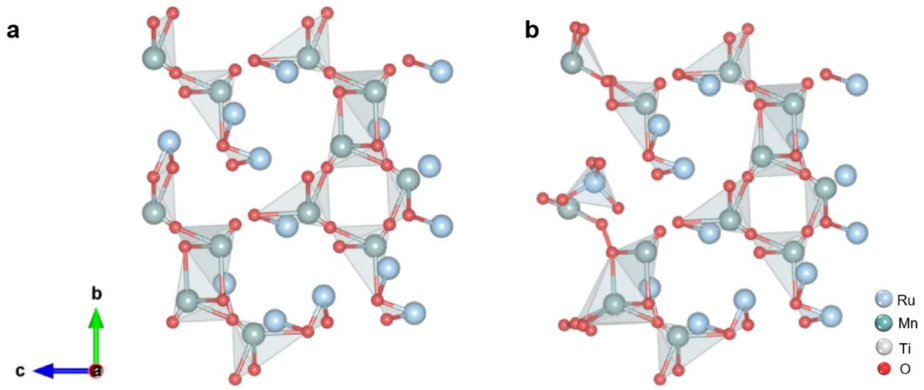

Supplementary Figure 38. $RuMnO_x$ catalyst model for first principles calculations. a,**b**, Atomic structure of as-constructed (**a**) and optimized (**b**) $Ru_{0.56}Mn_{0.44}O_2$.

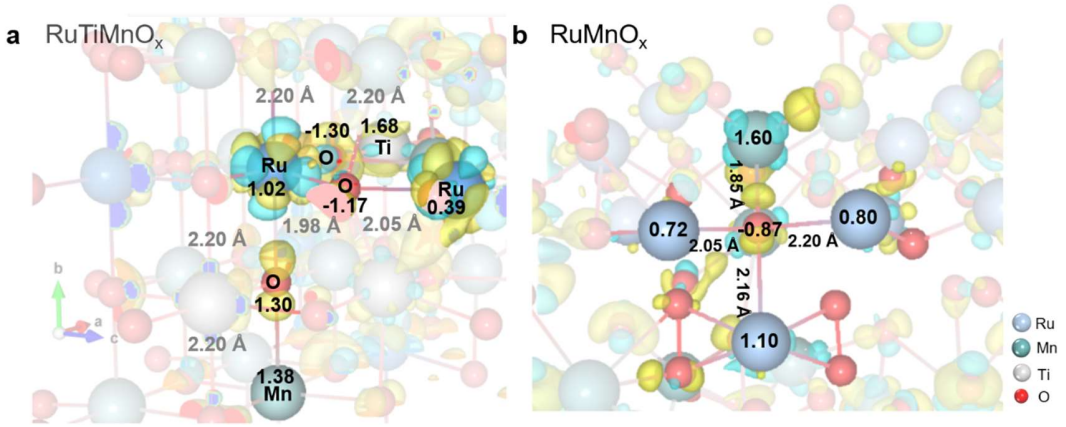

Supplementary Figure 39. Charge density difference analysis. a,**b**, The charge density difference between $Ru_{0.24}Ti_{0.28}Mn_{0.48}O$ (**a**) and $Ru_{0.56}Mn_{0.44}O_2$ (**b**). The values of Bader charge (in black) and bond length (in gray) are labeled.

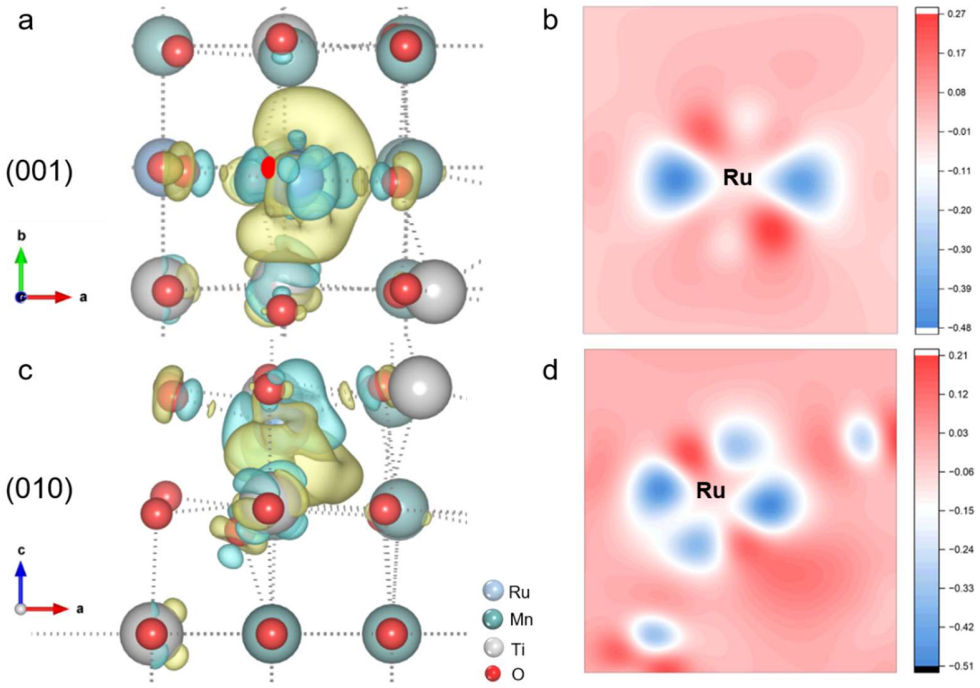

Supplementary Figure 40. Charge density difference analysis of $Ru_{0.24}Ti_{0.28}Mn_{0.48}O$. Differential charge density analysis of $Ru_{0.24}Ti_{0.28}Mn_{0.48}O$ (001) (**a**,**b**) and (010) (**c**,**d**). The blue and yellow shaded area mean the electron density accumulation and donation.

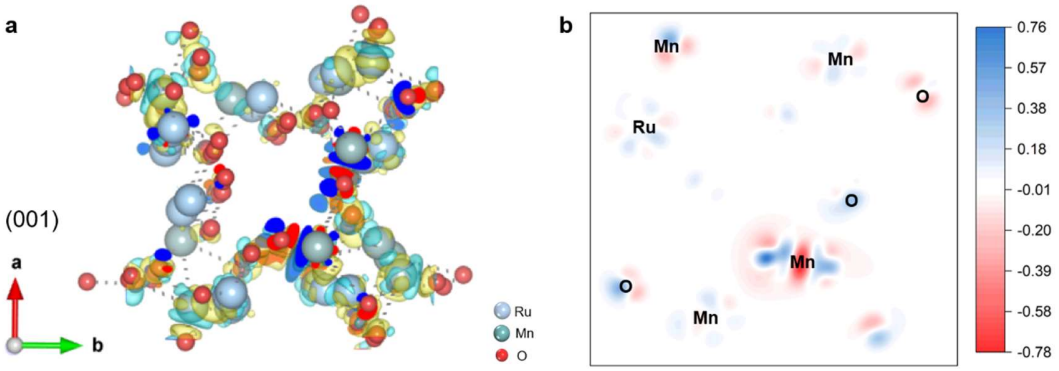

Supplementary Figure 41. Charge density difference analysis of $Ru_{0.56}Mn_{0.44}O_2$. a,**b**, Differential charge density analysis of $Ru_{0.56}Mn_{0.44}O_2$ (001). The blue and yellow shaded area mean the electron density accumulation and donation.

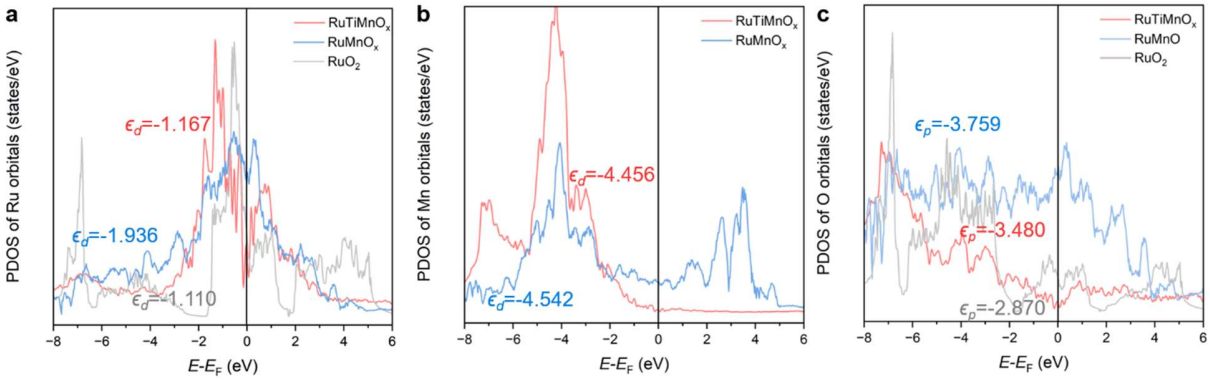

Supplementary Figure 42. Projected density of states (PDOS) analysis. a–**c**, PDOS and band center of Ru orbitals (**a**), Mn orbitals (**b**) and O orbitals (**c**) for $Ru_{0.24}Ti_{0.28}Mn_{0.48}O$, $Ru_{0.56}Mn_{0.44}O_2$ and RuO_2.

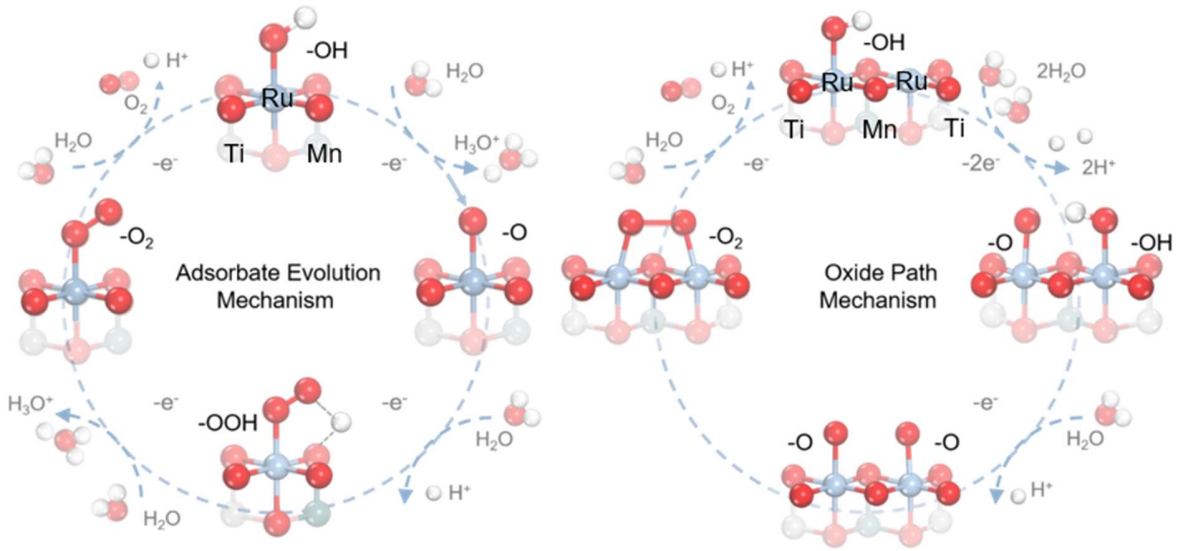

Supplementary Figure 43. Schematic diagram of the OER mechanism on $RuTiMnO_x$.

Schematic illustration of simplified OER mechanism of adsorbate evolution mechanism (AEM) and oxide path mechanism (OPM) on $RuTiMnO_x$.

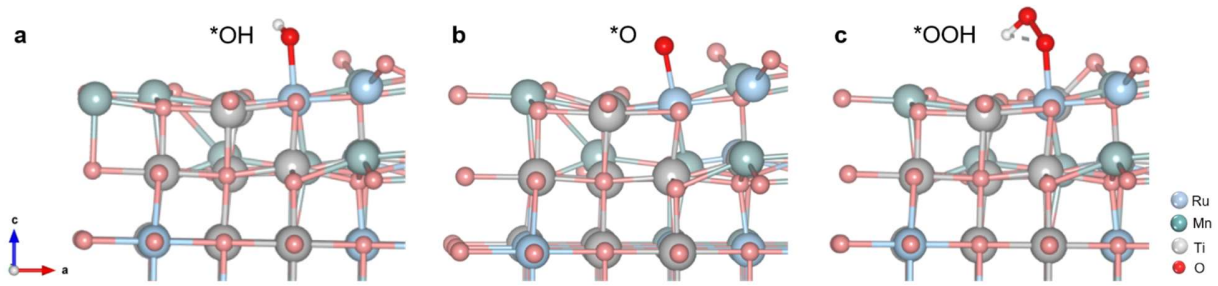

Supplementary Figure 44. $RuTiMnO_x$ model adsorbed with OER intermediates in AEM pathway. Side view of $Ru_{0.24}Ti_{0.28}Mn_{0.48}O$ with adsorbed intermediate of *OH (**a**), *O (**b**), and *OOH (**b**) on the interfacial Ru site.

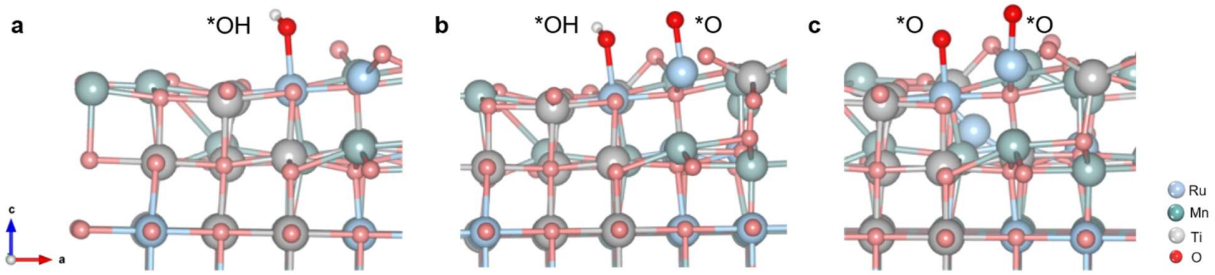

Supplementary Figure 45. $RuTiMnO_x$ model adsorbed with OER intermediates in OPM pathway. Side view of $Ru_{0.24}Ti_{0.28}Mn_{0.48}O$ with adsorbed intermediate of *OH (**a**), *OH + *O (**b**), and *O + *O (**c**) on the interfacial Ru site.

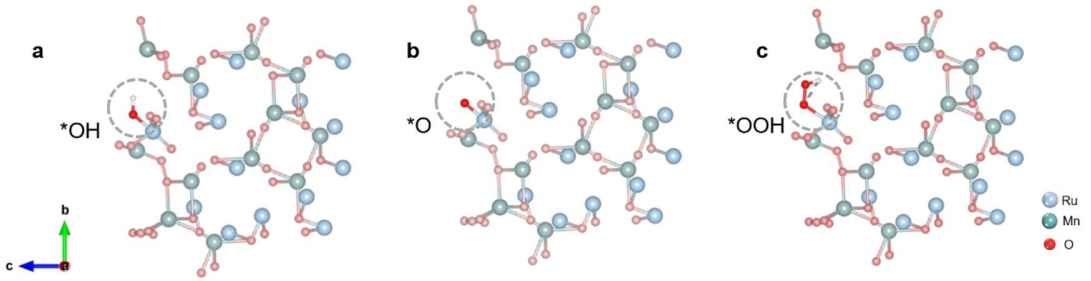

Supplementary Figure 46. $RuMnO_x$ model adsorbed with OER intermediates in AEM pathway. Side view of $Ru_{0.56}Mn_{0.44}O_2$ with adsorbed intermediate of *OH (**a**), *O (**b**), and *OOH (**b**) on the interfacial Ru site.

Supplementary Table 1. Summary of the OER activity and stability of $RuTiMnO_x$ electrodes with different proportions.

OER activity is represented by overpotential η (mV) and OER stability is represented by deactivation rate ΔE (mV h^{-1}) to drive 10 mA cm^{-2}.

Sample	Ru%	Ti%	Mn%	η (mV)	ΔE (mV/h)
RuO_2	100	0	0	209.479	93.6215
$Ru_{0.87}Ti_{0.02}Mn_{0.11}O_x$	87.23	2.43	11.04	200.54	38.265
$Ru_{0.74}Ti_{0.08}Mn_{0.18}O_x$	73.56	8.08	18.36	189.879	17.5175
$Ru_{0.63}Ti_{0.12}Mn_{0.25}O_x$	63.02	12.04	24.94	186.513	10.0505
$Ru_{0.51}Ti_{0.18}Mn_{0.31}O_x$	51.45	17.63	30.92	188.121	8.3795
$Ru_{0.32}Ti_{0.46}Mn_{0.22}O_x$	32.68	21.66	45.66	175.433	4.474
$Ru_{0.28}Ti_{0.19}Mn_{0.53}O_x$	28.43	52.9	18.67	172.817	2.5395
$Ru_{0.18}Ti_{0.46}Mn_{0.36}O_x$	18.38	45.94	35.68	194.464	6.173
$Ru_{0.17}Ti_{0.21}Mn_{0.62}O_x$	17.12	62.37	20.51	205.161	3.2315

Supplementary Table 2. The detailed parameters corresponding to the adopted back-propagation neural network.

Total parameters: 11,410, trainable parameters: 11,410.

Layer (type)	Output shape	Trainable parameters
dense_25 (Dense)	(None, 128)	512
dense_26 (Dense)	(None, 64)	8,256
dense_27 (Dense)	(None, 32)	2,080
dense_28 (Dense)	(None, 16)	528
dense_29 (Dense)	(None, 2)	34

Supplementary Table 3. **Lattice parameters of $Ru_{0.24}Ti_{0.28}Mn_{0.48}O$ obtained by XRD Rietveld refinement.**

Formula	$Ru_{0.24}Ti_{0.28}Mn_{0.48}O$
Crystal system	Cubic
Space group	F m -3 m
a/Å	4.4038
b/Å	4.4038
c/Å	4.4038
α	90°
β	90°
γ	90°
Cell volume/ $Å^3$	85.403

Supplementary Table 4. Lattice parameters of $Ru_{0.56}Mn_{0.44}O_2$ obtained by XRD Rietveld refinement.

Formula	$Ru_{0.56}Mn_{0.44}O_2$
Crystal system	Tetragonal
Space group	I 4/m
a/Å	10.034
b/Å	10.034
c/Å	2.886
α	90°
β	90°
γ	90°
Cell volume/ $Å^3$	290.558

Supplementary Table 5. OER intrinsic comparison in different electrolytes.

OER mass activity and ECSA-normalized current densities (j_{ECSA}) comparison at 1.53 V vs. RHE of $RuTiMnO_x$, $RuMnO_x$, and Com. RuO_2 in 0.5 M H_2SO_4 (pH=0), 0.5 M PBS (pH=7), and 1.0 M KOH (pH=14), respectively.

Sample	Mass activity (A g_{Ru}^{-1}) @ 1.53 V vs. RHE			j_{ECSA} (mA/cm^2) @ 1.53 V vs. RHE		
	pH = 0	pH = 7	pH = 14	pH = 0	pH = 7	pH = 14
$RuTiMnO_x$	4249.3	1613.61	5115.81	1.18	0.37	1.24
$RuMnO_x$	313.72	90.31	615.14	0.27	0.07	0.43
RuO_2	87.57	14.30	68.62	0.20	0.03	0.15

Supplementary Table 6. Activity and stability comparisons with reported state-of-the-art electrocatalysts in acidic media.

The activity is summarized in terms of overpotential under 10 mA cm^{-2} (η_{10}). The stability is summarized in terms of duration time under 10 mA cm^{-2}.

Sample	η_{10} (mV)	Duration Time (h) @ 10 mA cm^{-2}	Electrolyte		Ref
$RuTiMnO_x$	165.2	3000	0.5 M H_2SO_4		This work
$RuMnO_x$	180.5	14	0.5 M H_2SO_4		This work
RuO_2	224.1	4	0.5 M H_2SO_4		This work
$CoWO_4$-delaminated	288	175	0.5 M H_2SO_4	[7]	*Science* **384**, 1373 (2024)
LMCF (La and Mn-codoped cobalt spinel fibers)	370	360	0.1 M $HClO_4$	[8]	*Science* **380**, 609 (2023)
$12Ru/MnO_2$	161	200	0.1 M $HClO_4$	[9]	*Nat. Catal*. **4**, 1012 (2021)
Ni-RuO_2	214	200	0.1 M $HClO_4$	[10]	*Nat. Mater*. **22**, 100 (2023)
Ru/Ti_4O_7	150	500	0.5 M H_2SO_4	[11]	*Nat. Commun*. **15**, 2728 (2024)
Ru array-Co_3O_4	160	1500	0.5 M H_2SO_4	[12]	*J. Am. Chem. Soc*., **146**, 12958 (2024)
$Ta_xTm_yIr_{1-x-y}O_{2-\delta}$	198	500	0.5 M H_2SO_4	[13]	*Nat. Nanotechnol*. **16**, 1371 (2021)
Sr-$IrMnO_2$/CNTs	236	400	0.5 M H_2SO_4	[14]	*Adv. Mater*. **36**, 2306934 (2024)
Ir_1-Co_3O_4	227	90	0.5 M H_2SO_4	[15]	*Adv. Mater.* 2401163 (2024)
Ir/WO_3/CC	249	36	0.5 M H_2SO_4	[16]	*Angew. Chem. Int. Ed*. **63**, e202406947 (2024)
MD-RuO_2-BN (multiscale defective RuO_2 bicontinuous nanoreactor)	196	24	0.5 M H_2SO_4	[17]	*Nat. Commun*. **15**, 3928 (2024)
Ru-VO_2	228	60	0.5 M H_2SO_4	[18]	*Adv. Mater*. **36**, 2310690 (2024)

Supplementary Table 7. Activity and stability comparisons with reported state-of-the-art electrocatalysts in neutral media.

The activity is summarized in terms of overpotential under 10 mA cm^{-2} (η_{10}). The stability is summarized in terms of duration time under 10 mA cm^{-2}.

Sample	η_{10} (mV)	Duration Time (h) @ 10 mA cm^{-2}	electrolyte	Ref
$RuTiMnO_x$	233.5	1500	0.5 M PBS	This work
$RuMnO_x$	256.3	15	0.5 M PBS	This work
RuO_2	335.4	5	0.5 M PBS	This work
Ru-VO_2	269	60	1.0 M PBS	[18] *Adv. Mater*. **36**, 2310690 (2024)
Ni-$FeWO_4$@WO_3/NF	235	200	1.0 M PBS	[19] *Adv. Mater*. **36**, 2308925 (2024)
ZnFeNiCuCoRu-O	270	20	1.0 M PBS	[20] *Adv. Mater.* **36**, 2308490 (2024)
Ir-CoFe LDHs	323	24	1.0 M PBS	[21] *Nano Lett*. **23**, 5092-5100 (2023)
RuO_2/CoO_x	240	200	1.0 M PBS	[22] *Nat. Commun*. **13**, 5448 (2022)
IrO_2/V_2O_5	329	20	1.0 M PBS	[23] *Adv. Sci*. **9**, 2104636 (2022)
Sm-$LaCoO_3$	530	50	1.0 M PBS	[24] *J. Am. Chem. Soc*. **144**, 13163 (2022)

Supplementary Table 8. Activity and stability comparisons with reported state-of-the-art electrocatalysts in alkaline media.

The activity is summarized in terms of overpotential under 10 mA cm^{-2} (η_{10}). The stability is summarized in terms of duration time under 10 mA cm^{-2}.

Sample	η_{10} (mV)	Duration Time (h) @ 10 mA cm^{-2}	electrolyte		Ref
$RuTiMnO_x$	185.6	2000	1.0 M KOH		This work
$RuMnO_x$	211.2	20	1.0 M KOH		This work
RuO_2	239.6	10	1.0 M KOH		This work
$FeCo{-}N_3O_3$@C	298	240	0.1 M KOH	[25]	*Nat. Synth*. **3**, 878-890 (2024)
$RuZn\text{-}Co_3O_4$	172	100	1.0 M KOH	[26]	*Angew. Chem. Int. Ed*. **63**, e202407509 (2024)
$(FeCoNiCrCu)Se_x$	222	1000	1.0 M KOH	[27]	*Joule* **8**, 2342-2356 (2024)
Ru/Ti_4O_7	180	300	1.0 M KOH	[11]	*Nat. Commun*. **15**, 2728 (2024)
ZnFeNiCuCoRu-O	170	30	1.0 M KOH	[20]	*Adv. Mater*. **36**, 2308490 (2024)
Ru/Co-N-C	276	20	1.0 M KOH	[28]	*Adv. Mater*. **34**, 2110103 (2022)
high-entropy single-atom (HESA)	270	10 @ 1.53 V	0.1 M KOH	[29]	*Nat. Sustain.* **6**, 816-826 (2023)
W-718a	320±10	48 @ 5 mA cm^{-2}	0.1 M KOH	[30]	*Nat. Mater*. **23**, 252-261 (2024)

Supplementary Table 9. Summary of Ru K-edge adsorption energy (E_0) and valence states for $RuTiMnO_x$, $RuMnO_x$, Ru foil and RuO_2. Related to Supplementary Fig. 23a.

	E_0	Valence
$RuTiMnO_x$	22117.6	+3.3
$RuMnO_x$	22116.8	+3.4
Ru foil	22107.2	0
RuO_2	22119.6	+4

Supplementary Table 10. Summary of Mn K-edge E_0 and valence states for $RuTiMnO_x$, $RuMnO_x$, Mn foil, Mn_2O_3 and MnO_2. Related to Supplementary Fig. 23b.

	E_0	Valence
$RuTiMnO_x$	6552.2	+2.59
$RuMnO_x$	6552.32	+2.66
Mn foil	6539	0
Mn_2O_3	6554.61	+3
MnO_2	6558.449	+4

Supplementary Table 11. EXAFS fitting parameters at the Ru K-edge for $RuTiMnO_x$ and RuO_2.

Sample	Shell	Coordination number (CN)	Bond length R (Å)	σ^2 (Å)×10 $^{-3}$	ΔE_0 (eV)	R factor
$RuTiMnO_x$	Ru-O1	3.5	1.99	6.53	5.65	0.021
	Ru-O2	2.2	2.39	3.15	2.11	
	Ru-M	3.1	2.70	4.51	4.82	
RuO_2	Ru-O	6	1.98	1.48	1.30	0.011

Notes: [a]*CN*: coordination numbers; [b]*R*: bond distance; [c]σ^2: Debye-Waller factors; [d] ΔE_0: the inner potential correction. *R* factor: goodness of fit.

Supplementary Table 12. Summary of in-situ Mn K-edge XANES E_0 and valence states for $RuTiMnO_x$. Related to Supplementary Fig. 27.

	E_0	Valence
ex-situ	6551.0	+2.40
+V-15 min	6551.2	+2.44
+V-30 min	6552.2	+2.64
-V-15 min	6551.3	+2.46

Supplementary Table 13. Summary of de-metallization energies.

The calculated de-metallization energies for Ru in RuO_2; Ru and Mn in $RuTiMnO_x$ and $RuMnO_x$. Related to Fig. 6f.

	De-metallization energy
$RuTiMnO_x$-Ru	1.8984
$RuTiMnO_x$-Mn	2.0516
$RuMnO_x$-Ru	1.4360
$RuMnO_x$-Mn	1.8176
RuO_2-Ru	1.7510

References

1. Y. Ren *et al.* Locally Ordered Single-Atom Catalysts for Electrocatalysis. *Angew. Chem. Int. Ed.* **63**, e202315003 (2024).
2. K. D. France, Z. Zeng, T. Wu & G. TNyström, Functional materials from nanocellulose: utilizing structure–property relationships in bottom-up fabrication. *Adv. Mater.* **33**, 2000657 (2021).
3. L. Sun *et al*. Chemical vapour deposition. *Nat. Rev. Methods Primers* **1**, 5 (2021).
4. Q. Wang *et al*. Atomic-scale engineering of chemical-vapor-deposition-grown 2D transition metal dichalcogenides for electrocatalysis. *Energy Environ. Sci.* **13**, 1593–1616 (2020).
5. S. Yadav & A. Sharma, Importance and challenges of hydrothermal technique for synthesis of transition metal oxides and composites as supercapacitor electrode materials. *J. Energy Storage* **44**, 103295 (2021).
6. N. Nandihalli, D. H. Gregory & T. Mori, Energy-saving pathways for thermoelectric nanomaterial synthesis: hydrothermal/solvothermal, microwave-assisted, solution-based, and powder processing. *Adv. Sci.* **9**, 2106052 (2022).
7. R. Ram *et al.* Water-hydroxide trapping in cobalt tungstate for proton exchange membrane water electrolysis. *Science* **384**, 1373–1380 (2024).
8. L. Chong *et al.* La-and Mn-doped cobalt spinel oxygen evolution catalyst for proton exchange membrane electrolysis. *Science* **380**, 609–616 (2023).
9. C. Lin *et al.* In-situ reconstructed Ru atom array on α-MnO_2 with enhanced performance for acidic water oxidation. *Nat. Catal.* **4**, 1012–1023 (2021).
10. Z.-Y. Wu *et al.* Non-iridium-based electrocatalyst for durable acidic oxygen evolution reaction in proton exchange membrane water electrolysis. *Nat. Mater.* **22**, 100–108 (2023).

11. S. Zhao *et al*. Constructing regulable supports via non-stoichiometric engineering to stabilize ruthenium nanoparticles for enhanced pH-universal water splitting. *Nat. Commun*. **15**, 2728 (2024).
12. J. Chang *et al.* Oxygen radical coupling on short-range ordered Ru atom arrays enables exceptional activity and stability for acidic water oxidation. *J. Am. Chem. Soc.* **146**, 12958-12968 (2024).
13. S. Hao *et al*. Torsion strained iridium oxide for efficient acidic water oxidation in proton exchange membrane electrolyzers. *Nat. Nanotechnol.* **16**, 1371–1377 (2021).
14. J. Kuang, B. Deng, Z. Jiang, Y. Wang & Z. J. Jiang, Sr-stabilized $IrMnO_2$ solid solution nano-electrocatalysts with superior activity and excellent durability for oxygen evolution reaction in acid media. *Adv. Mater.* **36**, 2306934 (2024).
15. S. Kaushik *et al*. Universal synthesis of single-atom catalysts by direct thermal decomposition of molten salts for boosting acidic water splitting. *Adv. Mater.* **36**, 2401163 (2024).
16. W. Wang *et al*. Enrooted-type metal-support interaction boosting oxygen evolution reaction in acidic media. *Angew. Chem. Int. Ed.* **136**, e202406947 (2024).
17. D. Chen *et al*. Bicontinuous RuO_2 nanoreactors for acidic water oxidation. *Nat. Commun.* **15**, 3928 (2024).
18. Z. Niu *et al*. Robust Ru-VO_2 bifunctional catalysts for all-pH overall water splitting. *Adv. Mater.* **36**, 2310690 (2024).
19. S. Zhao *et al*. Lewis acid driving asymmetric interfacial electron distribution to stabilize active species for efficient neutral water oxidation. *Adv. Mater.* **36**, 2308925 (2024).
20. K. Miao *et al.* Hollow-structured and polyhedron-shaped high entropy oxide toward highly active and robust oxygen evolution reaction in a full ph range. *Adv. Mater.* **36**, 2308490 (2024).

21. J. M. Yu *et al*. High-performance electrochemical and photoelectrochemical water splitting at neutral pH by Ir nanocluster-anchored CoFe-layered double hydroxide nanosheets. *Nano Lett.* **23**, 5092–5100 (2023).

22. K. Du *et al*. Interface engineering breaks both stability and activity limits of RuO_2 for sustainable water oxidation. *Nat. Commun.* **13**, 5448 (2022).

23. X. Zheng *et al*. Strong oxide-support interaction over IrO_2/V_2O_5 for efficient pH-universal water splitting. *Adv. Sci.* **9**, 2104636 (2022).

24. Z.-Y. Yu *et al*. General synthesis of tube-like nanostructured perovskite oxides with tunable transition metal-oxygen covalency for efficient water electrooxidation in neutral media. *J. Am. Chem. Soc.* **144**, 13163-13173 (2022).

25. B. Tang *et al*. A Janus dual-atom catalyst for electrocatalytic oxygen reduction and evolution. *Nat. Synth.* **3**, 878–890 (2024).

26. S. Chu *et al*. Selective activation of lattice oxygen site through coordination engineering to boost the activity and stability of oxygen evolution reaction. *Angew. Chem. Int. Ed.* **63**, e202407509 (2024).

27. F. Qian *et al*. Asymmetric active sites originate from high-entropy metal selenides by Joule heating to boost electrocatalytic water oxidation. *Joule* **8**, 2342–2356 (2024).

28. C. Rong *et al.* Electronic structure engineering of single-atom Ru sites via Co-N_4 sites for bifunctional pH-universal water splitting. *Adv. Mater.* **34**, 2110103 (2022).

29. X. Lei *et al*. High-entropy single-atom activated carbon catalysts for sustainable oxygen electrocatalysis. *Nat. Sustain.* **6**, 816–826 (2023).

30. L. Magnier *et al*. Fe-Ni-based alloys as highly active and low-cost oxygen evolution reaction catalyst in alkaline media. *Nat. Mater.* **23**, 252–261 (2024).